

MASTER'S THESIS

**Jet-Fragmentation Transverse Momentum
from Di-Hadrons Correlations in
 $\sqrt{s_{NN}} = 5.02$ TeV Pb-Pb Collisions.**

Author:
Alexander Kevin Gilbert

Supervisor:
Sami Räsänen

Department of Physics

June 22, 2020



JYVÄSKYLÄN YLIOPISTO
UNIVERSITY OF JYVÄSKYLÄ

Preface

In the vast universe that floating around without purpose in the seemingly infinite emptiness, I questioned myself, "Why does the universe exist?" A rather philosophical question that is beyond science since it can only answer "how" partly but not "why". Even the answer to "how" itself is not perfect and complete yet. Thus provide an opportunity for many generations to develop science and unlock the truth behind mystery of the universe's existence. But as we uncover more explanation, we came into realization that we are all just quarks and leptons, bounded together to form atoms and create complex organic molecules to build up a sentient life form. Is there any meaning to life? Maybe universe exist without any specific purpose or reason and our existence is just some cosmic accident which is very unlikely to occur. We may end up living a meaningless live if we search the meaning of life itself. But it does not necessarily stop us to have a purpose. There is no meaning of life until we create one. And thus our life become meaningful after fulfilling our purpose. This thesis is presented to serve my purpose as a physicist: to unravel how the nature works. It is written to finish my master degree and thus will help me to serve my greater purpose in life later on for the better humanity and the balance of nature.

I would like to thank ALICE collaboration for collecting the data in which this thesis is built around. Thanks to Dong Jo Kim for offering me this thesis topic. As the progress continue, thanks to Sami Räsänen who had supervised my work. Back in summer 2019, I was a newbie in programming. But thanks to Oskari Saarimäki who helped me to boost up my coding skill from zero to the level where I can write independently my own program for this thesis. My programming skill is not perfect yet, but I know how to learn and improve it. I also would like to thank Heidi Rytönen for some ROOT commands advice. Thanks to Juusi Viinikainen for some discussion we have on his code. Thanks to Jyväskylän Yliopisto for giving me scholarship and covering my living expense during my study. Without the funding, it would be impossible for me to finish my degree. Thanks also to Kari J. Eskola for some discussion about perturbative QCD. And finally, thanks also to my mother and people who donated to me so I could finally arrive in Finland.

Jyväskylä
June 22, 2020

Abstract

Jet-Fragmentation Transverse Momentum from Di-Hadrons Correlations in $\sqrt{s_{NN}} = 5.02$ TeV Pb-Pb Collisions.

The jets' transverse structure in Pb-Pb collision system has been studied with jet-fragmentation transverse momentum (j_T) distribution. The data were collected from ALICE experiment at LHC in energy $\sqrt{s_{NN}} = 5.02$ TeV per nucleon. The analysis was conducted on centrality classes 0-10%, 10-20%, 20-40%, and 40-60% and trigger particle transverse momentum $3 < p_{Tt} < 25$ GeV/c. The j_T signal shows Gaussian distribution (narrow component) related to non-perturbative hadronization and inverse gamma distribution (wide component) related to quantum chromodynamics (QCD) splitting. The measurement of yield per trigger particle results shows a decreasing trend as p_{Tt} grows and the decline becomes sharper from peripheral to central collision, proving the enhancement of low- p_T particle production due to high-multiplicity environment in heavy ion collision and jet energy loss inside hot quark-gluon plasma. The width of narrow component is independent of p_{Tt} and centrality class, proving that the hadronization is universal process. On the other hand, the width for wide component shows fluctuation over p_{Tt} . The results are compared to AMPT 2 simulation, ALICE experiment pp $\sqrt{s} = 5.02$ TeV and 7 TeV data. The comparison to pp data set shows high-multiplicity environment and medium modification in Pb-Pb, while the comparison to AMPT 2 shows overestimation of minijet parton production at low p_{Tt} .

Keywords: two-particle correlation, jet-fragmentation transverse momentum, perturbative QCD (pQCD), jet energy loss, jet quenching, heavy-ion collision, quark-gluon plasma (QGP), QGP medium, flow, ALICE experiment.

Contents

Preface	iii
Abstract	v
1 Introduction	1
2 Theoretical Bases	3
2.1 QCD Showering	3
2.2 Hadronization	5
2.3 Heavy Ion Physics	5
2.3.1 Centrality	5
2.3.2 Flow	8
2.3.3 Jet Quenching	10
3 Experimental And Monte-Carlo Instruments	13
3.1 CERN	13
3.1.1 ALICE	15
3.2 AMPT 2 Simulation	18
4 Data Description	19
4.1 Event Selection	19
4.2 Track Selection	19
5 Analysis	21
5.1 Two-Particle Correlation	21
5.2 Signal Extraction	22
5.3 Fitting j_T Signal	24
5.4 Finding the RMS of j_T and yield per trigger particles	26
5.5 Comparison Between Different Centrality And Different Collision System	26
6 Results	27
6.1 Results for RMS of j_T and Yield per Trigger Particle	27
6.2 Comparison To pp Data	29
6.3 Comparison To AMPT 2 Model	31
7 Conclusions And Insights	35
A Approximation of Medium Formation Timescale Compared to Nuclear Radius	45
B Cut-Off Limit of j_T Distributions	47
C Pb-Pb j_T signal distributions	51

1 Introduction

Since 1960's, quantum chromodynamics (QCD) [1] has been developed to explain the substructure of baryons and mesons, together called as hadron. Baryon consists of three valence quarks each with three different colors. Meson consists of a valence quark and a valence antiquark with their corresponding color and anticolor. These quarks are bounded together by gluon, a vector boson that carries color charges. But they are confined inside color-neutral hadrons at low temperatures and thus makes them hard to observe. With the current collider technology, we can heat up hadrons by colliding nuclei at ultrarelativistic speed and start to deconfine them. As a result, we can produce a droplet of strongly interacting matter called quark-gluon-plasma (QGP) [2]. Figure 1.1 shows the current understanding of QCD phase diagram. The minimum temperature of QGP production is roughly 150 MeV. This value is nearly three million times the temperature of the sun's surface which makes QGP not just an ordinary "plasma". It is assumed that the QGP naturally exist a few microseconds after big bang [3] and now we can study its properties by reproducing it in ultrarelativistic heavy ion collisions.

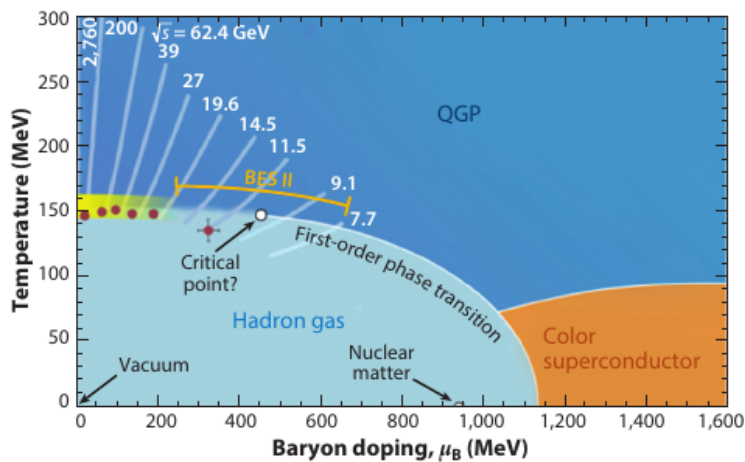


Figure 1.1: At very high temperature, quarks and gluons start to deconfine and form QGP. As the temperature cools down, they start to hadronize into nucleons via crossover phase transition if the baryon doping μ_B is below critical point. Otherwise, they go through first-order phase transition. At very high μ_B and low temperature like in neutron stars, nucleons are squeezed until they are no longer separated individuals and become color superconductor. Figure from [2].

In heavy ion collisions, partons (quarks or gluons) carry out some fraction of their nucleon's energy. This energy is not necessarily distributed equally among them. High-energy partons create jets upon impact and low-energy partons thermalize into QGP medium. The dense QGP in approximate local thermal equilibrium is well described with relativistic hydrodynamics [4] and expands before it turns into thermal hadron gas and streaming freely into vacuum. Jets that traverse the medium, for example like the "subleading" jet in Figure 1.2, will lose some of its energy and radiate

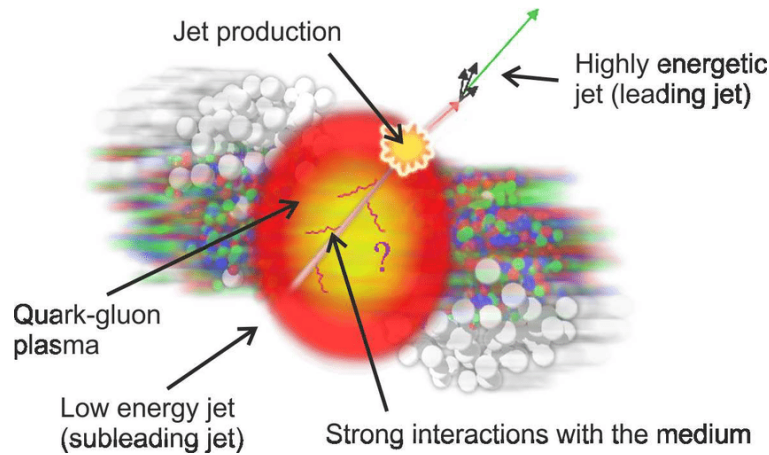


Figure 1.2: Illustration of heavy ion collision. Subleading jet is quenched through its way out from medium. Figure from [14].

gluons at broader angle. These phenomena is called jet quenching [5], first observed in Relativistic Heavy Ion Collider (RHIC) [6, 7] and later at CERN [8, 9, 10, 11].

During its journey from collision vertex to the detector, jets get fragmented. For example, in PYTHIA simulation [12], the fragmentation consists of two-step processes. The first process is the perturbative process where parton radiates soft gluons. The second process is the non-perturbative hadronization modeled by Lund string fragmentation model [13]. Earlier study in proton-proton (pp) and proton-lead (p-Pb) collision systems[15, 16] shows that these two process can be treated as two additive functions from two-particle or di-hadron correlation. In this thesis, I apply the similar analysis in reference [15, 16] to lead-lead (Pb-Pb) collision system as a function of centrality class. I will do the background subtraction from jet-fragmentation transverse momentum (j_T) distribution from ALICE experiment data in order to extract the j_T signal. Then I fit the Gaussian and inverse gamma function to the j_T signal in order to find the yield per trigger and root mean square of j_T . The results are then compared to pp system to find any medium modification in transverse structure of jet fragmentation. And finally, I also compare the results from experiment to AMPT model [17, 18, 19, 20].

In heavy ion environment, more nucleons are involved in collision. Consequently, it provides more entropy and bulks of QGP are more easily produced, especially in central collision. Meanwhile in pp and p-Pb systems, even though it is possible that QGP presents in both systems [21, 22], a significant amount of QGP is hardly formed to suppress jet's energy. It would be interesting to see how the presence of medium affect jets. Hence study of jet-fragmentation transverse momentum in Pb-Pb collision system provide an opportunity to observe their correlation. The choice to use di-hadron correlation approach instead of full jet reconstruction was made because it is more sensitive to soft radiation and hadronization part in jet fragmentation [23, 24].

This thesis consist of seven chapters. The first chapter is a brief introduction to heavy ion collision and the purpose of this thesis. The second chapter provides the theoretical bases around the topic. The third chapter is about the experimental instruments that are used to collect data. The fourth chapter provides data description and the fifth chapter explains the data analysis in details. The sixth chapter presents the results along with its explanations and the conclusions are drawn in chapter seven along with some insights for future study.

2 Theoretical Bases

As the heavy ions move toward each other at ultrarelativistic speed, they are Lorentz contracted, causing the ball-shaped nuclei turn into flat pancake. This initial state is purely kinematical. The dynamic process begin at the moment of collision and can be studied with perturbative QCD (pQCD). Later on, the partons hadronize into bound-states particles through non-perturbative process. An interesting observable that can be measured in heavy ion collision is centrality which affect how much the medium produced from a certain collision type. There are also several heavy ion physics phenomena observed due to the presence of hot QGP medium such as flow and jet quenching. We will discuss these more detail in the following sections.

2.1 QCD Showering

At high-energy scale where the momentum transfer Q^2 is much larger than QCD scale Λ_{QCD} , pQCD become applicable. Hard partons can split into softer particles by radiating gluon through branching process $q \rightarrow qg$ or $g \rightarrow gg$. In case if the hard parton is gluon, quark-antiquark pair creation $g \rightarrow q\bar{q}$ is also possible. Any soft/collinear splitting from the hard parton has probability density

$$d\mathcal{P}_a(z, Q^2) = \frac{dQ^2}{Q^2} \frac{\alpha_s}{2\pi} P_{a \rightarrow bc}(z) dz \Delta_s(Q_{max}^2, Q^2). \quad (2.1)$$

This equation is well known as DGLAP evolution equation [25, 26, 27], where α_s is the running strong-interaction coupling constant [28], $\Delta_s(Q_{max}^2, Q^2)$ is Sudakov form factor, $P_{a \rightarrow bc}(z)$ is the splitting function for a process where the mother particle a split into the daughter particles b and c , z is the fraction of momentum carried away by particle b from particle a , and thus $(1-z)$ is the fraction of momentum carried away by particle c . Since there are three possible branching processes, the splitting function for each process are

$$P_{q \rightarrow qg}(z) = \frac{4}{3} \frac{1+z^2}{1-z}, \quad (2.2)$$

$$P_{g \rightarrow gg}(z) = 3 \frac{(1-z(1-z))^2}{z(1-z)}, \quad (2.3)$$

$$P_{g \rightarrow q\bar{q}}(z) = \frac{n_f}{2} (z^2 + (1-z)^2), \quad (2.4)$$

with n_f is the number of flavors that are kinematically allowed. The Sudakov form factor is given by [29]

$$\Delta_s(Q_{max}^2, Q^2) = \exp \left\{ - \int_Q^{Q_{max}^2} \frac{dk^2}{k^2} \int_{z_{min}}^{z_{max}} dz \frac{\alpha_s(z, k^2)}{2\pi} P_{a \rightarrow bc}(z) \right\} \quad (2.5)$$

with k now is the integration variable for momentum transfer. The DGLAP evolution equation gives probability that the emission occurs first time at transition from scale

Q_{max}^2 to Q^2 . Therefore it gives probability that there is no emission in the middle of transition. After the hard parton reach scale Q^2 , it can emit another soft quark/gluon again. This process is repeated until the hard parton reach the cutoff scale Q_0^2 . Since $\alpha_s \propto 1/\ln(Q^2/\Lambda_{QCD}^2)$, it will become infinite when $Q^2 = \Lambda_{QCD}$. The Λ_{QCD} typically is in order of hundreds MeV so it is safe to set the cutoff scale to order of 1 GeV. After Q_0^2 scale is reached, the α_s become large and perturbative approach is no longer applicable. The non-perturbative hadronization then takes over the next process. (Note that the final state partons may still scatter with each other before hadronization as we shall see in Section 2.3.3.)

During its evolution to the cutoff scale, soft gluon splitting radiated from parton may occur and follow the angular ordered cascade pattern [30]. This pattern is a consequence of uncertainty principle and time dilation. For example, assume the splitting $q \rightarrow q\bar{q}$ after $g \rightarrow q\bar{q}$ like in the leftmost process of Figure 2.1. The quark

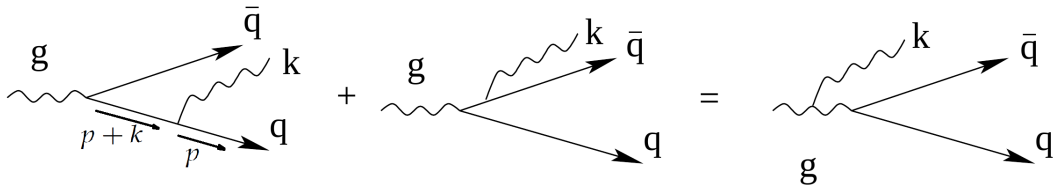


Figure 2.1: The soft gluon k emission out off q or \bar{q} acts as if it came off the on-shell parent gluon g . Figure from [30] with some editing.

carries energy E_q according to laboratory frame. But since the quark is not moving according to its own frame, then its energy in quark's frame $E'_q \sim M_{virt}$, with M_{virt} is its virtual mass. Thus it follows that the formation time of gluon with four-momentum k is

$$t_{form} = \gamma t_{virt} \approx \frac{E_q}{M_{virt}} \frac{1}{2E'_q} \approx \frac{E_q}{2M_{virt}^2} \approx \frac{E_q}{2(p+k)^2}. \quad (2.6)$$

In the denominator, since $p^2 + k^2 \ll 2p \cdot k$ at ultrarelativistic limit, the only term remain is $2p \cdot k = 2(E_p E_k - |\vec{p}||\vec{k}| \cos \theta_{qg})$, with θ_{qg} is a small angle between quark and gluon. The splitting occurs with assumption that the gluon is soft so it almost does not change the initial energy of quark, thus $E_p \approx E_q$. Taking the Taylor expansion of the cosine and equating $E_k = |\vec{k}|$, we have

$$t_{form} \approx \frac{E_q}{2|\vec{k}|E_p \theta_{qg}^2} \approx \frac{1}{2|\vec{k}|\theta_{qg}^2} \approx \frac{\lambda_{\perp}}{\theta_{qg}}, \quad (2.7)$$

with the last approximation comes after substituting the transverse wavelength of the radiated gluon $\lambda_{\perp}^{-1} \approx 2k_{\perp} \approx 2|\vec{k}|\theta_{qg}$. Meanwhile, the $q\bar{q}$ system moves apart during the gluon formation time at transverse distance

$$r_{\perp} \approx \theta_{q\bar{q}} t_{form} \approx \lambda_{\perp} \frac{\theta_{q\bar{q}}}{\theta_{qg}}, \quad (2.8)$$

with $\theta_{q\bar{q}}$ is the small angle between $q\bar{q}$ pair. Since the transverse wavelength of the radiated gluon λ_{\perp} must be smaller than the transverse separation r_{\perp} , therefore it is necessary that $\theta_{q\bar{q}} > \theta_{qg}$. If such a radiation would produce $\theta_{q\bar{q}} < \theta_{qg}$, the process would be suppressed and the splitting occurred through $g \rightarrow gg$ process beforehand like in the rightmost diagram of Figure 2.1.

2.2 Hadronization

Once the cutoff energy scale Q_0^2 is reached, the perturbative process ends and partons must hadronize into final bound-state particles. There are several model for hadronization and one of them is the Lund string fragmentation model [13] used in PYTHIA event generator [12]. This model is a building block for this thesis analysis.

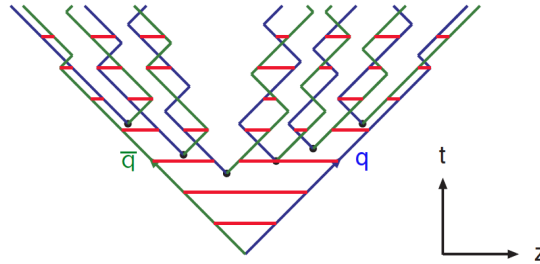


Figure 2.2: Illustration of string model for parton fragmentation. The figure is presented in light cone representation. The quark-antiquark pair is assumed to move at speed of light to different directions. Figure from [31].

In PYTHIA simulation, one can imagine a quark-antiquark pair exchanging gluons like illustration in Figure 2.2. As they move farther from each other, their kinetic energy is converted to potential energy due to color confinement. At some point, the gluon string break and produce another pair of quark-antiquark. This new pair also moves to different direction and break the string again to produce another quark-antiquark pair. The process is repeated until the pair production is no longer kinematically allowed. In this case, the final state particles are meson. In case of baryon production, the string breaks into diquark-antidiquark pair instead of quark-antiquark pair. The probability of breaking the string is defined by the Lund symmetric fragmentation function [13];

$$f(z) \propto \frac{1}{z} (1-z)^a \exp\left(-\frac{bE_T^2}{z}\right), \quad (2.9)$$

with z is the fraction of momentum given to hadron from system, a and b are tuneable parameter in the model, and $E_T = \sqrt{m^2 + p_T^2}$ is transverse energy of the hadron. m^2 is the mass of hadron and the transverse momentum p_T is perpendicular with respect to string axis. After all hadron are created, the short-lifetime particles still can decay and generate the final state hadrons in simulation.

Later in this thesis, the experiment data is compared to AMPT model [17, 18, 19, 20] where the same hadronization model is also applied. In addition to Lund string fragmentation model, the second version of AMPT simulation also includes "rehadronization" modeled by quark coalescence model [32, 33, 34, 35]. The details about AMPT will be discussed in Chapter 3.

2.3 Heavy Ion Physics

2.3.1 Centrality

Out of many collisions events, some of ions may collide centrally, some of them may barely scratch at the edge of nuclei, and other collisions may vary in between. Figures 2.3a shows cross-sectional view of two nuclei from opposite z -directions. The

overlap region between nuclei is the region where collision occurs. The more central the collision, the larger the overlap area and hence the more nucleons participate in collision. Other nucleons outside the overlap region do not collide and thus only become the spectators of the collision. To quantify how central the collision is, impact parameter b is introduced as a transverse distance between the center of two overlap nuclei. Value of b ranges from zero at the most central collision to twice of nucleus radius R at the most peripheral collision for similar nuclei.

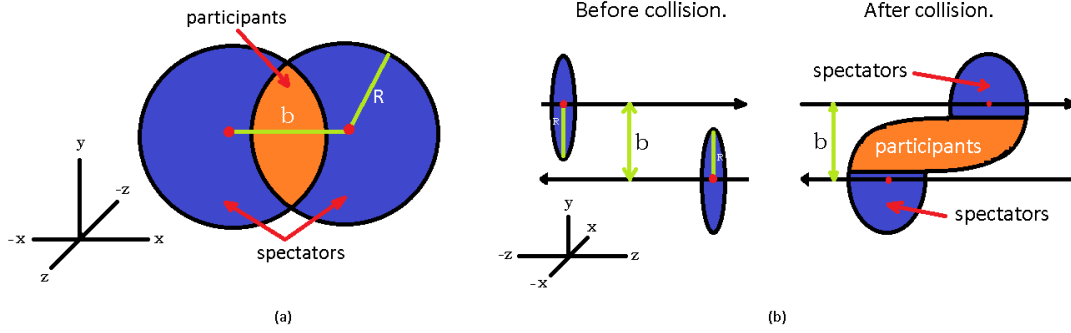


Figure 2.3: (a) Cross-sectional illustration of the incoming nuclei. (b) Chronological order of the collision viewed from side view.

However, the impact parameter can not be measured since our detectors can only detect the final state particles created after collision. As demonstrated in Figure 2.3b, the spectators go ahead but the participants lag behind because they interact with other participants in front of them. Thus the measurable observables related to impact parameter are the multiplicity of charged particles N_{ch} that come out from participants and the energy deposited in detectors by spectators. However, some spectator nuclei remain undetected inside beam pipeline after peripheral collision [36]. Therefore centrality determination mainly relies on multiplicity while the result from spectators energy measurement in central collision serves as a complement.

In order to drawing connection between the measured multiplicity in experiment with impact parameter, ALICE collaboration in reference [36] implemented Monte Carlo (MC) method to Glauber model. First, they modeled stochastically the nucleons positions inside each nucleus using modified Wood-Saxon nuclear density function

$$\rho(r) = \rho_0 \frac{1 + w(r/R)^2}{1 + \exp(\frac{r-R}{a})}. \quad (2.10)$$

For ^{208}Pb , the nuclear radius $R = (6.62 \pm 0.06)$ fm and its skin thickness $a = (0.546 \pm 0.010)$ fm. Parameter w characterizes deviations from the spherical shape. For Pb-Pb, parameter w is set to zero. The nucleon density parameter ρ_0 is obtained from normalization condition $\int \rho(r) dr^3 = A$. Each nucleon has distance $d_{min} = (0.4 \pm 0.4)$ fm between their centers. The second step is simulating the nuclear collision by varying impact parameter. In this simulation, number of collision N_{coll} and number of participants N_{part} are deduced from Glauber model by counting how many binary nucleon-nucleon collisions and how many the nucleons that collide at least once respectively. Here, number of "ancestors" (the sources that emit particles independently) is parameterized under assumption

$$N_{ancestors} = f \cdot N_{part} + (1 - f) \cdot N_{coll}, \quad (2.11)$$

with parameter $0 < f < 1$ is a fraction of soft interactions in medium and $1 - f$ gives

the remaining fraction of hard interactions that produce jets. The number of particles produced per interaction is generated using negative binomial distribution (NBD)

$$P_{\mu,k}(n) = \frac{\Gamma(n+k)}{\Gamma(n+1)\Gamma(k)} \cdot \frac{(\mu/k)^n}{(\mu/k+1)^{n+k}}, \quad (2.12)$$

with n is number of hits per ancestor, μ is the mean multiplicity per ancestor, and parameter k controls the width. $P_{\mu,k}(n) \cdot N_{ancestors}$ is fitted to the multiplicity distribution obtained from experiment. Figure 2.4 shows the result of fitting. In x-axis, V0 amplitude is directly proportional to N_{ch} . The larger N_{ch} , the smaller b , and thus the more central the collision. Y-axis is proportional to number of events per multiplicity dN_{evt}/dN_{ch} . As we can see in Figure 2.4, central collision events are much rarer but produce more charged particles and hence give very steep end in the distribution. Meanwhile, the less central events are more common but have less multiplicity.

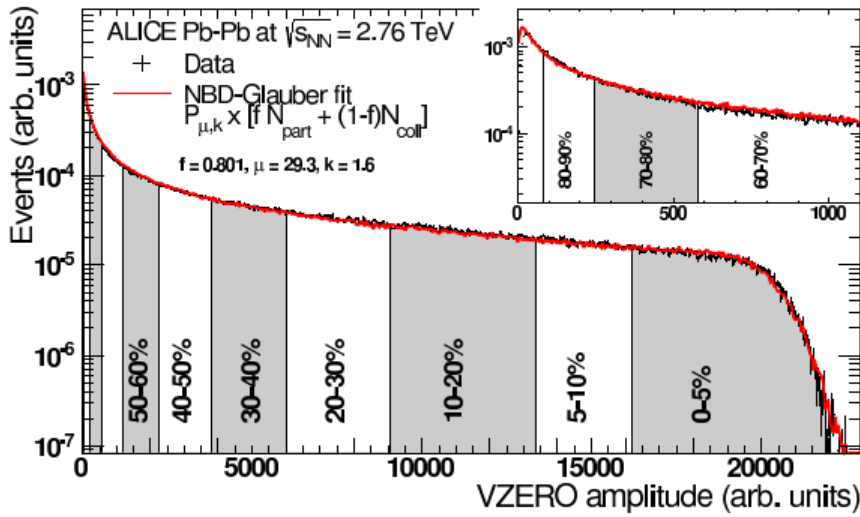


Figure 2.4: The multiplicity of charged particle distribution measured in ALICE. Figure from [36].

Since the range of impact parameter may vary for different nuclei, the same value of b in different collision system may represent different centrality. Hence, it is more convenient to present centrality as a percentile class [37] so it will be easier to compare centrality between different collision system. To present it, we define centrality percentile d as

$$d = \frac{\text{Area in some centrality percentage}}{\text{Total area}} \propto \frac{\int_{\infty}^{n_d} \frac{dN_{evt}}{dN_{ch}} dN_{ch}}{\int_{\infty}^{\infty} \frac{dN_{evt}}{dN_{ch}} dN_{ch}}. \quad (2.13)$$

For example, centrality class 0-5% in Figure 2.4 represents the top 5% of the *most central* collisions while 80-90% class represents the top 10-20% of the *most peripheral* collisions. The area of 0-5% class is 5% of the total area while the area of 80-90% class is 10% of the total area.

Nowadays, it is easy to determine the border of each class with ROOT once the distribution is obtained. Let us take an example from Figures 2.4 again. First, we find the total area of distribution by taking the its integral from the last bin to zero. Then

starting from the most central class, we can obtain the area of the most central class by multiplying the total area with $d = 5\%$. In order to find the first border $n_{5\%}$, we can loop backward the integral from the last bin to some arbitrary number of bin and compare the result of integration to the area of the current class. Once the result of integration matches the fractional area, break the loop and we can find in which bin the border is contained. And finally, we can repeat the same procedure to find the next borders starting from the result obtained from the previous border. For example, in Figure 2.4, the second border is at

$$\begin{aligned}
 d = 10\% &\propto \frac{\int_{\infty}^{n_{10\%}} \frac{dN_{evt}}{dN_{ch}} dN_{ch}}{\int_{\infty}^0 \frac{dN_{evt}}{dN_{ch}} dN_{ch}} = \frac{1}{\int_{\infty}^0 \frac{dN_{evt}}{dN_{ch}} dN_{ch}} \left(\int_{\infty}^{n_{5\%}} \frac{dN_{evt}}{dN_{ch}} dN_{ch} + \int_{n_{5\%}}^{n_{10\%}} \frac{dN_{evt}}{dN_{ch}} dN_{ch} \right) \\
 &\propto 5\% + \frac{\int_{\infty}^{n_{10\%}} \frac{dN_{evt}}{dN_{ch}} dN_{ch}}{\int_{\infty}^0 \frac{dN_{evt}}{dN_{ch}} dN_{ch}} \\
 \therefore 10\% - 5\% &\propto \frac{\int_{n_{5\%}}^{n_{10\%}} \frac{dN_{evt}}{dN_{ch}} dN_{ch}}{\int_{\infty}^0 \frac{dN_{evt}}{dN_{ch}} dN_{ch}} \propto \frac{\text{Area of 5-10\% class}}{\text{Total area}}. \tag{2.14}
 \end{aligned}$$

Here we can use the bin that contain $n_{5\%}$ from the previous result to find the bin that contain $n_{10\%}$ and the mapping of centrality border is continued iteratively. In analysis, the events are classified with several centrality classes and we will see the comparison between jet-fragmentation transverse momentum in central and peripheral collision.

2.3.2 Flow

After QGP medium is created, it expands due to thermal expansion and the surrounding vacuum pressure. In central collision, the medium expands radially, creating a radial flow. In non-central collision, this expansion is anisotropic because momenta of the constituent particles in medium are not distributed equally. Figure 2.5 illustrates why the elliptic "rugby-ball" medium has tendency to flow anisotropically. The medium nearby reaction plane is hotter than the parts of the medium that are further away from reaction plane. Consequently, higher spatial momentum distribution in reaction plane causes in-plane expansion is more rapid than out-of-plane expansion. How the expansion evolves over time is presented in Figure 2.6. Because of the gap between expansion rates, the overall medium shape turns from elliptic into a nearly symmetric circle viewed from transverse plane.

The anisotropic flow can be expressed as a Fourier expansion of invariant triple differential distribution [38]

$$E \frac{d^3N}{d^3\vec{p}} = \frac{d^3N}{2\pi p_T dp_T dy} \left(1 + 2 \sum_{n=1}^{\infty} v_n \cos(n[\varphi - \Psi_{RP}]) \right), \tag{2.15}$$

with E is the particle energy, p_T is its transverse momentum, y is the rapidity of the particle, φ is the azimuthal angle, and Ψ_{RP} is the reaction plane angle. The sine terms cancel out because of symmetric expansion with respect to reaction plane. The

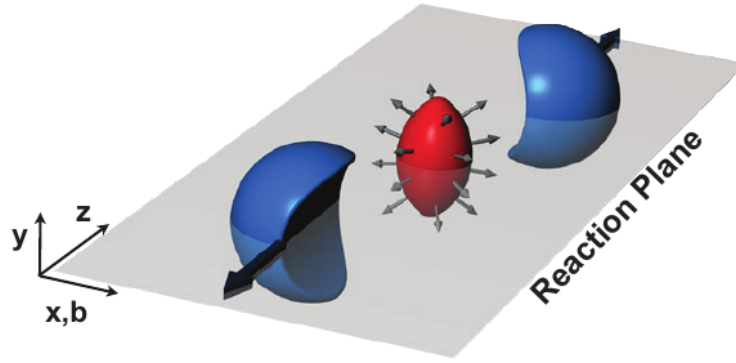


Figure 2.5: Illustration of peripheral collision. The impact parameter b and the beam axis z constitute the reaction plane. The arrows represent the spatial momentum flow. The rugby-ball-shaped medium expands anisotropically due to anisotropic momentum flow. Figure from [38].

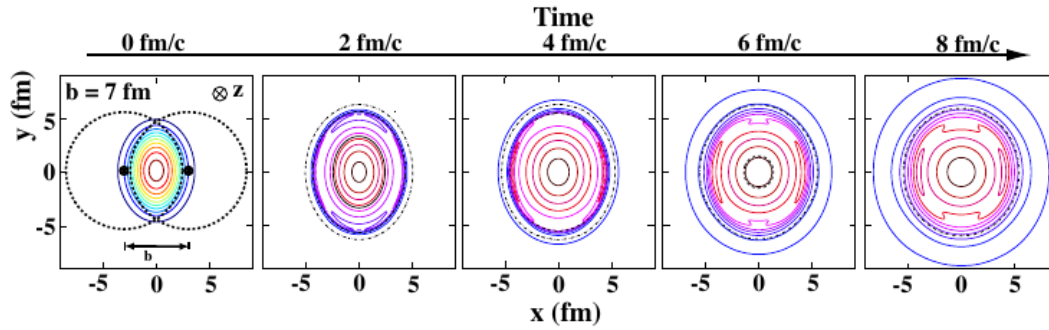


Figure 2.6: Evolution of QGP droplet in peripheral collision viewed from transverse plane. Figure from [38].

Fourier coefficient of the n^{th} harmonic is p_T and y dependent:

$$v_n(p_T, y) = \langle \cos(n[\varphi - \Psi_{RP}]) \rangle. \quad (2.16)$$

The angle bracket represents an average over all particles in all events within the given p_T and y . The first harmonic flow v_1 refers to directed flow which is caused by Coulomb repulsion between nuclei upon impact [39]. The second harmonic flow v_2 is elliptic (in non-central) or radial (in central) flow as a result of medium expansion. Since anisotropic expansion is greater in non-central collision, the value of v_2 in elliptic flow is more significant than in radial flow. The triangular flow v_3 comes from the fluctuation in number of participants in every event [40].

However, just like impact parameter, Ψ_{RP} currently can not be measured directly. One of several way to estimate the elliptic flow coefficient v_2 is using two-particle azimuthal correlation approach

$$\begin{aligned} \langle \langle e^{2i(\varphi_1 - \varphi_2)} \rangle \rangle &= \langle \langle e^{2i(\varphi_1 - \Psi_{RP} - (\varphi_2 - \Psi_{RP}))} \rangle \rangle \\ &= \langle \langle e^{2i(\varphi_1 - \Psi_{RP})} \rangle \langle e^{-2i(\varphi_2 - \Psi_{RP})} \rangle - \delta_2 \rangle \\ &= \langle v_2^2 + \delta_2 \rangle. \end{aligned} \quad (2.17)$$

The innermost angle brackets denote an average over all particles in an event and the outermost angle bracket denote an average over all events. This is true only if $v_2 \gg \delta_2$. Unfortunately, δ_2 is not negligible in general. I leave it here since the further

technical details are not directly related to this thesis. Interested readers can find further calculation in reference [38, 41]. The implication of flow phenomena to this thesis analysis is that the azimuthal structure become important later in the analysis.

2.3.3 Jet Quenching

Historically, the idea of jet quenching was proposed by Bjorken [5] in 1982. Upon collision, jets are formed first and later followed by creation of medium. But some jets still suffer the damping from medium because even if they move near to speed of light, they are still too late to escape from nuclear radius. A simple calculation using uncertainty principle to demonstrate this chronology is presented in Appendix A.

Experimentally, the early analysis of jet quenching is accessed with nuclear modification factor [42]

$$R_{AA}(p_T) = \frac{\frac{1}{N_{evt}^{AA}} \frac{d^2 N_{ch}^{AA}}{d\eta dp_T}}{\langle N_{col} \rangle \frac{1}{N_{evt}^{pp}} \frac{d^2 N_{ch}^{pp}}{d\eta dp_T}}. \quad (2.18)$$

It represents the ratio of charged particles yield between proton-proton (pp) and nucleus-nucleus (AA) systems scaled by average number of binary nucleon-nucleon collision $\langle N_{col} \rangle$. If there are no nuclear modifications including the presence of QGP in the heavy ion collision, one would expect the value of R_{AA} to be unity since nothing would be different between pp and AA systems. But the measurements of R_{AA} at RHIC [44, 43] and ALICE [45] presented in Figure 2.7 show that its value is not unity. The measured R_{AA} is p_T dependent and shows suppression of p_T more than 2 GeV/c.

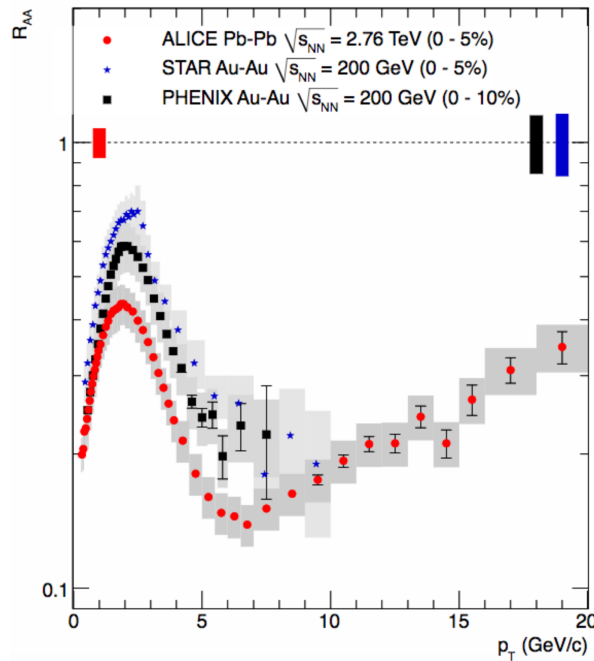


Figure 2.7: The R_{AA} measured in ALICE experiment at LHC compared to R_{AA} measurements from STAR and PHENIX experiments at RHIC. Figure from [45].

Another novel way to provide evidence of jet quenching is via the measurement of dijet imbalance [46]. When two hard partons collide in center of mass frame, they recoil in back-to-back direction. As previously illustrated in Figure 1.2, the

leading jet moving outward from QGP fireball and travel in vacuum space, while the subleading jet traverses the QGP medium, suffers energy loss, and produces more low-energy particles distributed on wider opening angle. The leading jet have more narrow opening angle and has more energy, causing geometrical and energy imbalance between both sides of jets. In ATLAS experiment, the dijet asymmetry is defined by

$$A_j = \frac{E_{T1} - E_{T2}}{E_{T1} + E_{T2}}, \Delta\phi > \frac{\pi}{2}, \quad (2.19)$$

with $E_{T1} > 100$ GeV is the transverse energy of the leading jet and $E_{T2} > 25$ GeV is the transverse energy of the subleading jet on the other side of leading jet's hemisphere. Figure 2.8 show the dijet asymmetry and azimuthal angle gap distribution at various centrality classes. If there is no asymmetry, A_j will always be zero and $\Delta\phi = \pi$. But

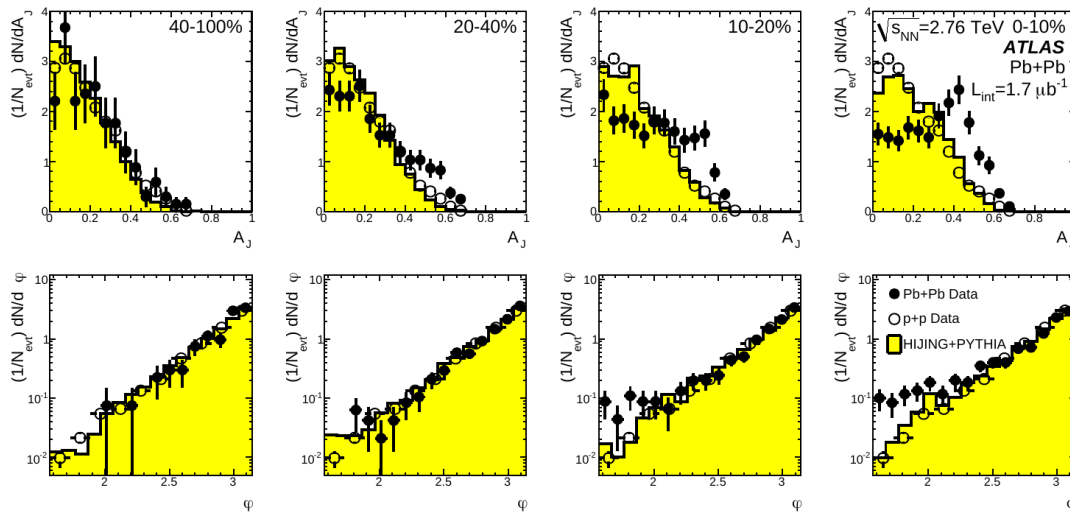


Figure 2.8: Top: Dijet asymmetry distribution from peripheral (right) to central (left) collision. The full circle is Pb-Pb data, the open circle is pp data, and the yellow histogram is PYTHIA+HIJING model simulation. Bottom: The dijet's azimuthal angle gap ($\Delta\phi$) distribution also in the same centrality class with the top figure. Figure from [46].

asymmetry indeed occurs even in pp data but the peak is relatively close to zero as compared to Pb-Pb data, especially in central collision which indicate more QGP produced and suppress further the subleading jet. $\Delta\phi$ distributions also show a rising deviation from π in Pb-Pb system as collisions become more central.

All these evidences raised questions on how the jets loss their energy and thus plenty of jet energy loss models are proposed. One of them is modeled with gluon splitting during jet's perturbative evolution like in Heavy Ion Jet Interaction Generator (HIJING) [47, 48, 49, 50] model. Another model like in A Multi-Phase Transport Model (AMPT) [17, 18, 19, 20] simulation modeled the jet energy loss by scattering of final state partons after the splitting process ends but right before hadronization. This scattering process in AMPT is called Zhang's Parton Cascade (ZPC) [51]. Currently, ZPC only consider scattering of $gg \rightarrow gg$ with the scattering cross section σ_{gg} is calculated from pQCD. Gluon-gluon scattering occurs whenever their closest distance is smaller than $\sqrt{\sigma_{gg}/\pi}$. The calculation result for the scattering gluon-gluon cross-section in this model is [51]

$$\sigma_{gg} \approx \frac{9\pi\alpha_s}{2\mu^2}, \quad (2.20)$$

with μ is the Debye screening mass generated by medium effect. Later in this thesis, the results from data experiment are compared with AMPT simulation to see how close (or far) this model to reality.

3 Experimental And Monte-Carlo Instruments

3.1 CERN

CERN's name is originally abbreviated from French name *Conseil européen pour la recherche nucléaire* which is then translated into European Organization for Nuclear Research. CERN was officially founded in 1954, but its origin came from 1949 pioneered by plenty of visionary scientists. After being torn apart by World Wars, European scientists, envisioned a laboratory where people can unite in the name of science for peace. This laboratory could also help them to share the increasing cost of nuclear research facilities [52]. Nowadays, CERN emphasize its mission to do science for peace and unite people around the world in pursuit of science [53, 54]. It has no concern with military-purpose research and keeps the scientific work published and open for everyone, which in return push more international collaborations. Currently CERN has 23 member states and many international research collaborations with non-member countries.

There are various researches carried out in CERN but most of the facilities, mainly the accelerators, are for particle physics research. As we can see in the Figure 3.1, Large Hadron Collider (LHC) itself already dominates the CERN area with its 27 km circumference, making it currently the largest particle accelerator in the world. But we can not simply drop any idle particle directly to LHC. In order to accelerate particles from zero to several TeV, it requires step-by-step progressive acceleration, and it's achieved by the smaller accelerator around it.

For Pb ions, the journey starts from injection of the heavy ions (Pb^{27+} , Pb^{28+} , or Pb^{29+}) [56, 57] from Electron Cyclotron Resonance (ECR) ion source into linear accelerator 3 (LINAC 3). The Pb ions are accelerated in LINAC 3 until they reach energy 4.2 MeV before passing stripper foil that strips away the heavy ions' electrons further to Pb^{54+} . The heavy ions are then transferred to Low Energy Ion Ring (LEIR). Inside LEIR, each long pulse from LINAC 3 is compressed into several "bunches" and accelerated further to 72 MeV. From LEIR, these bunches continue to Proton Synchrotron (PS) where they are accelerated to 5.9 GeV. As the size from each accelerator to the next one is getting bigger, more bunches can be loaded cumulatively. Certain numbers of bunches are called a "batch". The heavy ions are directed from PS to another stripper foil that strips all the remaining electrons before entering Super Proton Synchrotron (SPS). In SPS, these accumulated batches are accelerated again until 177 GeV. A further detail about how much the bunches and batches that are injected into every accelerator and its development can be read in reference [58]. And finally, the heavy-ion batches are unleashed into LHC in two opposite directions and accelerated until they reach center-of-mass energy $\sqrt{s_{NN}} = 5.02$ TeV.

For proton beam, it follows similar path but starts from LINAC 2 and Proton Synchrotron Booster (PSB) instead before entering PS. Proton beam energy is larger than Pb ion since its charge-to-mass ratio is smaller than Pb ion. By 2015, proton-proton center-of-mass energy collision can reach $\sqrt{s} = 13$ TeV.

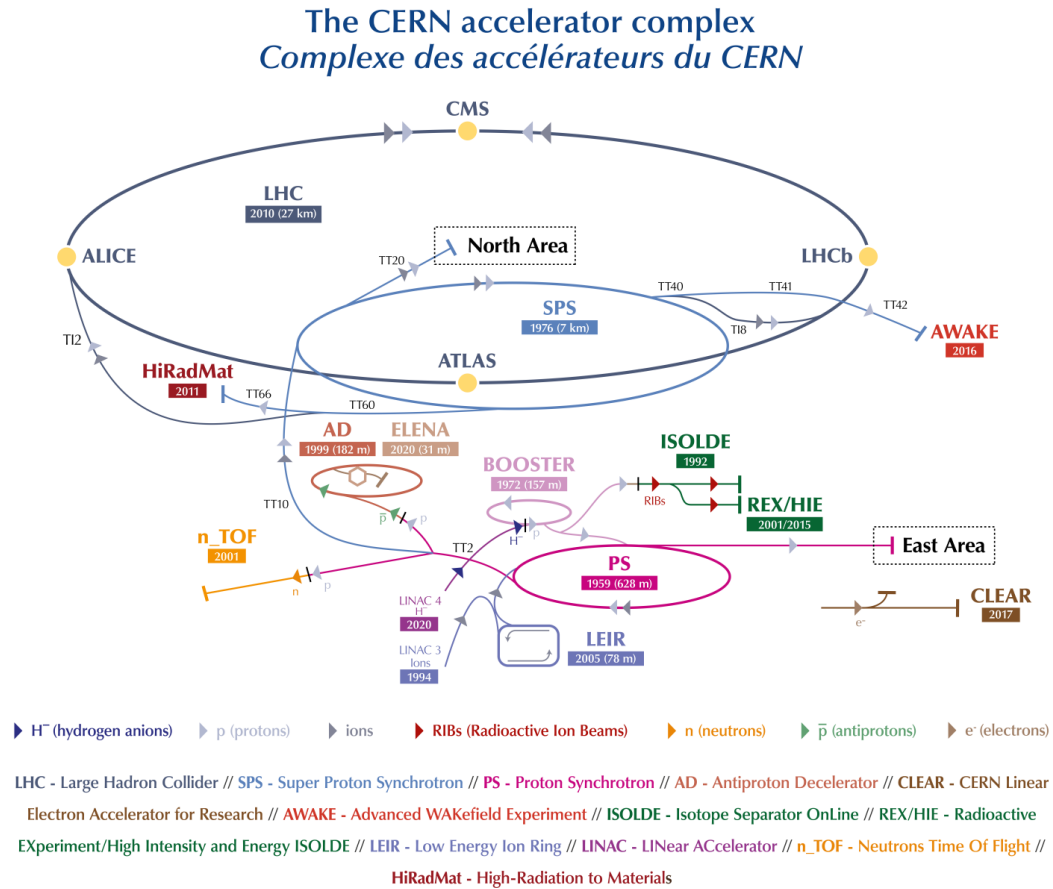


Figure 3.1: The latest CERN’s accelerators complex (2019). The accelerator route for heavy-ion beam’s starts from LINAC 3, LEIR, PS, SPS, and finally delivered to LHC to receive final acceleration. Figure from [55].

In order to accelerate particles, all accelerators are equipped with superconducting radio-frequency (RF) cavities [59]. To visualize how RF cavity works, consider a series of conductive rings arranged to be a linear pipeline, or toroidal circle in case of circular accelerator. Each ring is loaded with opposite charge next to each other. When protons pass the center of negatively-charged ring, it will be decelerated due to repulsion from positive charges inside the next ring and attraction from the current ring. By the same principle, when protons pass the center of positively-charged ring, it will receive boost toward negatively-charged ring in front of it. If the charges in every ring are switched to its opposite charge repeatedly at radio wave frequency (several MHz), the protons that are too slow will receive acceleration and other protons that are too fast will be slowed-down so they stay close together in one packet as a bunch. Thus the RF cavity works in such a way that charged particle inside beam pipeline will receive coulomb force due to modulated electric potential. At maximum energy, the beam will have zero acceleration and ready to be collided or injected to the bigger accelerator.

The accelerated particles still have to be directed to a place where detector is located. Superconducting magnets do this job, guiding particles to its collision site. In circular accelerators, dipole magnets are required to bend the bunches’ path into circular motion. Several higher-order multipole magnets like sextupole, octupole,

and decapole magnets are also used alongside the dipole magnets to correct the edges of dipole magnetic field in such a way so the magnetic field at the edges become straight. Quadrupole magnets are used in each accelerator to focus the beam either horizontally or vertically. Three quadrupole magnets can be arranged into an inner triplet [60]. These inner triplets are used to squeeze the particle bunches very tight right before they enter detector and hence increase the chance of collision.

Running electricity in RF cavity and electromagnet will rise heat because of electric resistance. To prevent this energy dissipation, all RF cavities and magnets are cooled with liquid helium until they become superconductor [59]. Without electric resistance, the accelerators can reach its maximum efficiency to generate electromagnetic field.

After the bunches collide, a lot of new particles are created and they hit a detector. Currently, there are eight detectors in LHC. They are A Toroidal LHC ApparatuS (ATLAS) [61], A Large Ion Collider Experiment (ALICE) [62], Compact Muon Solenoid (CMS) [63], TOTal Elastic and diffractive cross section Measurement (TOTEM) [64], Large Hadron Collider beauty (LHCb) [65], Large Hadron Collider forward (LHCf) [66], Monopole and Exotics Detector at the LHC (MoEDAL) [67], and ForwArD Search ExpeRiment (FASER) [68]. The data in this thesis was collected by the ALICE experiment.

3.1.1 ALICE

ALICE is a fusion of many detectors combined into a giant detector. Figure 3.2 shows how the layer-by-layer central-barrels detectors along with forward detectors and other components constitute the ALICE detector. At the core of ALICE's central-barrel detectors, there is a beam pipeline where collisions occur. After collision, some of the resulted particles pass the tracking detectors in central barrel where their tracks are reconstructed. The main tracking detectors consist of Inner Tracking System (ITS) and Time Projection Chamber (TPC).

ITS consists of Silicon Pixel Detector (SPD), Silicon Drift Detector (SDD), and Silicon Strip Detector (SSD). Each of them has two layer detector so there are six

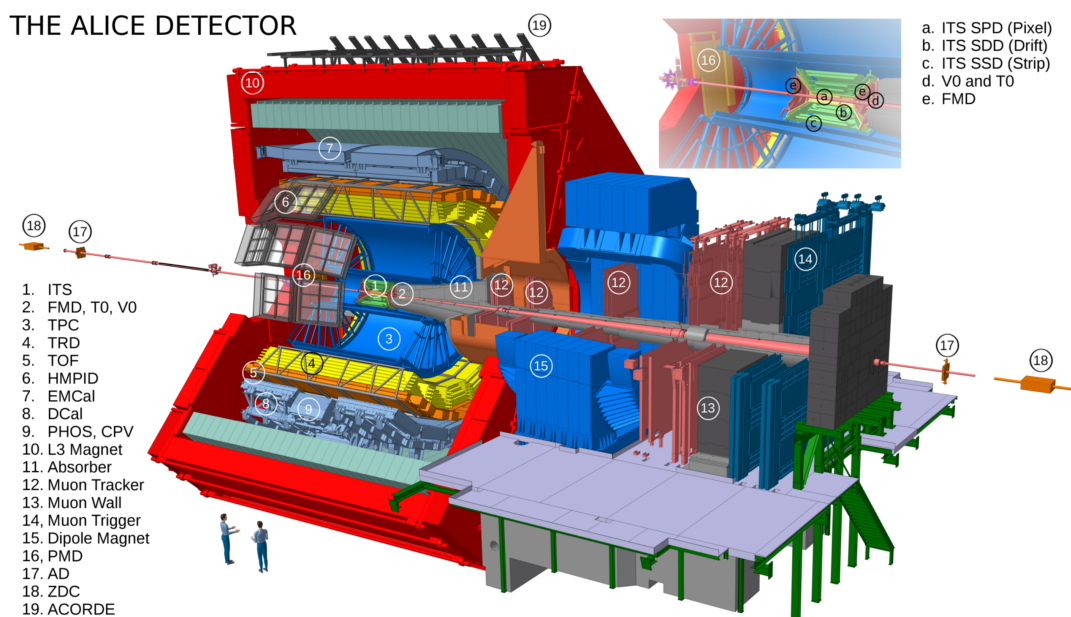


Figure 3.2: ALICE detectors design by the time Pb-Pb data experiment in 2015 was taken. Figure from [69].

layers of silicon detectors in ITS. As we can see in the zoomed part of Figure 3.2, the innermost part close to the beam pipe is SPD. Its task is to locate the vertex point in high-multiplicity environment. The next part is SDD. This detector was placed in the third and fourth layers because they have very high resolution two-dimensional sensors, making it suitable for high track-density experiments [70]. The outermost part of ITS is SSD. The SSD layers are crucial for the matching of tracks from the TPC to the ITS [71]. Beside determining particle's track, both SDD and SSD also measure energy loss per distance traveled dE/dx from low- p_T particle. From the measured dE/dx samples, ITS identifies what charged particles that passing through it.

Next to ITS, there is TPC detector [72] which is filled with $90 \text{ m}^3 \text{ Ne/CO}_2/\text{N}_2$ (90/10/5) gases. A voltage of 100 kV is generated to the gases so they will be easily ionized when a charged particle pass through them. The electrons that are knocked out from the gas molecules travel to the plates of multi-wire proportional chamber (MWPC) [73]. The maximum drift time for these electron is $90 \mu\text{s}$. TPC also measures dE/dx and thus also identifies particles.

The signals from TPC combined with ITS's signals give full track reconstruction. The reconstructed track provides information about the momentum of particle that has charge q . Since the presence of magnetic field B bends the charged particle's track, the particle's momentum can be obtained from relation $p = Bqr$ once the radius of track's curvature r is measured.

The next layers after TPC is Transition Radiation Detector (TRD) [74]. This detector consists of six-layer MWPCs filled with Xe-CO₂ gases, with fiber-foam coat in front of each chamber. Its main task is to identify particles, especially when there are two or more particles with the same energy. Since $E = \gamma mc^2$, heavier particles have smaller γ than lighter particle's γ at the same energy. The probability of transition radiation, when a charged particle across the boundary of material with different dielectric constant, is proportional to its γ . Thus when lighter charged particles traverse between fiber and foam, they emit more transition radiation. These radiation are then measured with MWPCs. Hence TRD can distinguish high-energy electron with other heavier particle like pion. TRD also measures dE/dx in combination with transition radiation measurement to identify particles.

The next layer is Time of Flight (TOF) detector [75]. It consists of stacked Multi-gap Resistive Plate Chambers (MRPC) placed with the same interval between them. TOF is used to measure the time of flight for the incoming particle to travel from interaction point to this detector with resolution of order 100 ps. TOF then calculates the velocity of particle. After the momentum of the particle is measured in the tracking detectors, the mass of the particle can be deduced from its velocity and momentum. The particle is then identified based on its mass.

The next layer is covered by two electromagnetic calorimeters, which consist of PHOSon Spectrometer (PHOS) [76] and ElectroMagnetic Calorimeter (EMCal) [77]. Unlike the previous central barrel detectors which cover the whole azimuthal angle, these calorimeters only cover $220^\circ < \varphi < 320^\circ$ for PHOS and $80^\circ < \varphi < 187^\circ$ for EMCal. PHOS is made of $17280 \text{ } 2.2 \times 2.2 \times 1.8 \text{ cm}^3 \text{ PbWO}_4$ scintillators coupled to large-area PIN-diodes with low-noise preamplifiers [76]. With this high granularity structure, PHOS is used to measure photons ($\sim 0.5\text{-}10 \text{ GeV}/c$), π^0 's ($\sim 1\text{-}10 \text{ GeV}/c$), and η mesons ($\sim 2\text{-}10 \text{ GeV}/c$). Meanwhile EMCal is used to measure a large fraction of jet energy up to $200 \text{ GeV}/c$ and beyond which includes charged particles, direct photons, and photons from particle decay, mostly dominated from decay $\pi^0 \rightarrow \gamma\gamma$ [77]. During years 2013-2015, EMCal was extended with Di-jet Calorimeter (DCal) [78] which increase the EMCal's azimuthal coverage at $260^\circ < \varphi < 320^\circ$, and hence providing partial back-to-back correlation measurement for jet quenching.

The outermost layer of central barrel is High-Momentum Particle Identification (HMPID) [79] with azimuthal coverage $1^\circ < \varphi < 59^\circ$. Its purpose is to identify charged hadron with momentum larger than 1 GeV/c. HMPID consists of ring-imaging Cherenkov counter (RICH) [80] detectors that contain C_6F_4 liquid and MWPC-based CsI photocathode. When an incoming particle traverse inside the C_6F_4 liquid, the particle will emit Cherenkov radiation if its velocity is greater than the phase velocity of light in that liquid. The photocathode then detects the radiation and measures its angle θ_c with respect to the particle's track. The particle's velocity v is then calculated from relation $v = c / [n \cos(\theta_c)]$, where n is a refractive index of C_6F_4 liquid. The particle's mass can be obtained by using the measured momentum before and the calculated velocity v .

All central detectors are encased by L3 solenoid magnet. On the top of the magnet, there is A COsmic Ray DEtector (ACORDE) [88]. This plastic-scintillator-based detector is used for measuring cosmic ray background and hence providing the standard for calibration. It is also used to study underground cosmic ray.

In forward direction along beam pipe, there are series of forward detectors. Some of them are placed on both sides of interaction point. Some of them are placed only one side at either A-side or C-side which refer to ATLAS side and CMS side at LHC tunnel respectively. All forward detectors can be moved along beam pipe.

The first three detectors [81] are T0, V0, and Forward Multiplicity Detector (FMD) located on both sides of interaction point. T0 is a Cherenkov counter-based detector for delivering the time and the longitudinal position of collision and for measuring the beam luminosity. V0 is plastic scintillator detectors located at $-3.7 < \eta < -1.7$ and $2.8 < \eta < 5.1$ to determine the trigger events and also to measure multiplicity of charged particles. And FMD is five rings silicon strip detectors to measure the charged particles multiplicity at $-3.4 < \eta < -1.7$ and $1.7 < \eta < 5.0$.

The next detector on A-side is Photon Multiplicity Detector (PMD) [82, 83]. It consists of small hexagonal gas-counter detectors arranged into honeycomb structure. This detector is located at $2.3 < \eta < 3.9$ to measure multiplicity of photons which mostly come from neutral pions decays.

The next detector on C-side is a muon spectrometer [84] which consists of a hadron absorber, five tracking chambers (Muon CHamber, MCH), an iron wall, and two trigger detectors (Muon TRigger, MTR). The purpose of this spectrometer is to measure the production of quarkonium (a meson made of a heavy quark-antiquark pair), light vector meson, and muon that comes from decay of heavy quark. The hadron absorber removes any background contamination from measurement. After that, the remaining particles go through five MCH stations each with MWPC-based two cathode pads. To further remove contamination from background, the iron wall (Muon Filter) is installed between the last MCH station and the first MTR station to remove leftover hadrons. The last parts are two MTR stations each with two resistive plate chambers providing trigger thresholds when muon pass through.

The next detector on both sides is ALICE diffractive detector (AD) [85, 86] which consists of two subdetectors ADA and ADC planted on both sides of interaction point. This detector is used to measure diffractive events where one or both of incoming particles break up after collision and scatter with large rapidity gap.

The last detectors is Zero-Degree Calorimeter (ZDC) [87]. This detector consists of two tungsten-quartz neutron calorimeters (ZN), two brass-quartz proton calorimeters (ZP), and two small electromagnetic calorimeter (ZEM). Both ZN and ZP pairs are placed about 112.5 m on both sides away from interaction point but ZEM is placed on C-side at around 7.35 m from interaction point. The purpose of ZDC is to determine centrality class by measuring the deposited energy from spectator nuclei [36].

3.2 AMPT 2 Simulation

In order to compare the results from ALICE experiment data with theoretical calculations, A Multi-Phase Transport Model (AMPT) [17, 18, 19, 20] simulation is used. Currently there are two major versions of the program: version 1. x and version 2. y , with x and y are integer number that are upgraded whenever the source codes are modified. Both version use different models and the differences are shown in Figure 3.3. In this thesis, the data from simulation are generated using the second version and will be called simply AMPT 2 data.

The simulation in AMPT 2 starts with setting up initial conditions using Heavy Ion Jet INteraction Generator (HIJING) [47, 48, 49, 50] model version 1.383 with jet quenching option is turned off. This model produces excited strings and minijet partons. In default model, the excited strings proceed directly through Lund string fragmentation [13]. The minijet partons undergo perturbative process until they reach cutoff scale Q_0^2 . For the jet quenching part, the final state partons from minijet partons are then scattering with each other governed by ZPC model [51]. Note that the cross section for $gg \rightarrow gg$ process here is also applied for (anti)quark-(anti)quark scattering [51, 89]. This makes the model to be oversimplified. After scatterings finish, they hadronize via Lund string fragmentation model.

Meanwhile in string melting model [89, 90, 91], the excited strings that already hadronize are transformed back into deconfined partons again. The converted partons then undergo scatterings with other partons using ZPC model whenever their closest distance less than $\sqrt{\sigma_{gg}/\pi}$. After all scatterings finish, these partons rehadronize with quark coalescence model which is similar to non-linear ALgebraic COalescence Rehadronization (ALCOR) [32, 33, 34, 35]. In this rehadronization model, two nearest quark-antiquark are simply tied up into meson and three (anti)quark are tied up into (anti)baryon.

The final part of both version is A Relativistic Transport (ART) model [92, 93] for modeling hadron cascade. This model includes baryon-baryon, baryon-meson, and meson-meson elastic and inelastic scatterings in superdense hadronic matter.

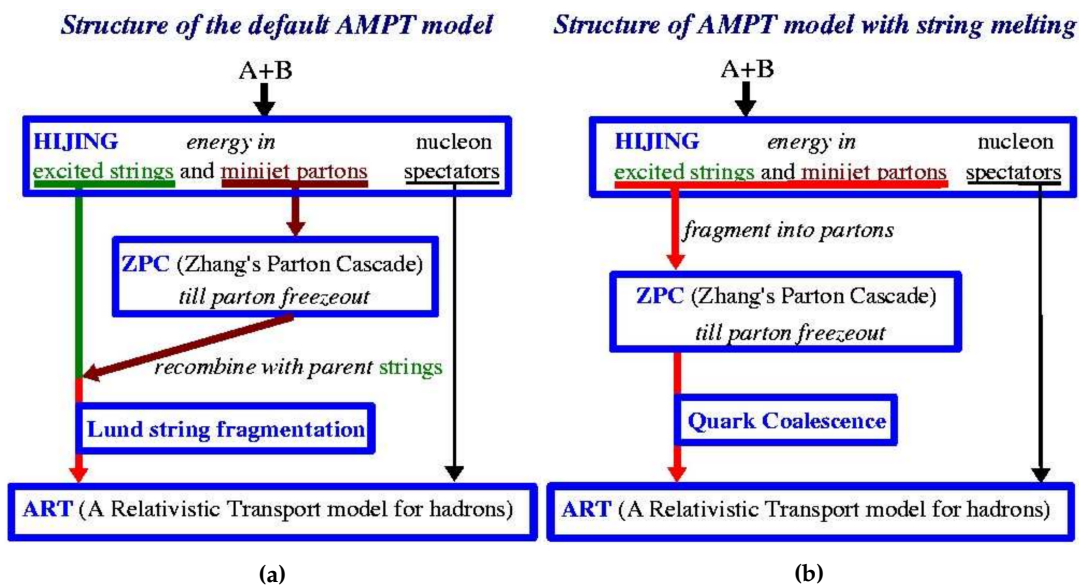


Figure 3.3: The simulation scheme of AMPT models in (a) default model, and in (b) string melting model. Figures from [19].

4 Data Description

The Monte Carlo data (MC) in this thesis is generated from AMPT 2 simulation with center-of-mass energy $\sqrt{s_{NN}} = 2.76$ TeV per nucleon. The real data for Pb-Pb system in this thesis was collected from ALICE experiment during Run-2 in years 2015. The center-of-mass energy for Pb-Pb system is $\sqrt{s_{NN}} = 5.02$ TeV per nucleon. The same analysis will be performed to both real and MC data. Due to limitation in data storage rates and capacity in experiment, trigger systems are needed to maximize the rare events recording and to suppress the background efficiently. Once the interesting events are recorded, the tracks of the particles can be reconstructed.

4.1 Event Selection

For Pb-Pb collision experiment in 2015, ALICE used three different trigger systems that run simultaneously: minimum bias (MB), centrality, and rare triggers [94]. Both MB and centrality triggers require signals from V0A, V0C, and both ZDC's to start recording. The strict MB trigger criteria for Pb-Pb system maximizes the acceptance from beam-beam interaction while rejecting beam-gas interaction due to leftover gas inside beam pipe. Beam-gas interactions give fake signals that come too early to either side of V0. Other source of background contamination is the interaction between the ions around the beam's halo and the machine structure itself. Rare trigger system is fired when MB trigger is fired and there is also a tuned signal from any other detector such as TRD, EMCal, Muon Spectrometer, and SPD.

4.2 Track Selection

Following the scheme in Figure 4.1, the central-barrel track reconstruction starts from "clusterization" in each detector. The result is a cluster of data that contain information such as positions, signal times, signal amplitudes, and any other properties. The next step is finding preliminary vertex of interaction from SPD cluster data. In this step, the vertex position is estimated using SPD only. This is done by extrapolating all pairs in SPD to find the point with the most intersections.

The next steps is track finding, marked with a sequence of blue boxes in Figure 4.1. It starts by matching clusters from TPC outermost layer with clusters from inner TPC layers. Then ITS matches the track information from TPC with its own clusters from outermost layer to innermost layer. A certain proximity cut is considered upon generating the track. The reconstructed track from TPC and ITS is then extrapolated to the most suitable preliminary vertex. From vertex found before, the track is then extrapolated outward and matched to the cluster found in detectors beyond TPC using Kalman filter technique [95]. After that, the new track is fitted inward again so the final vertex can be found more accurately.

The last step is finding the secondary vertex as result of photon conversion or decay of short-lived particle. The tracks are selected if their distance of closest approach (DCA) to the interaction vertex exceeding 1 mm for Pb-Pb. Then point of

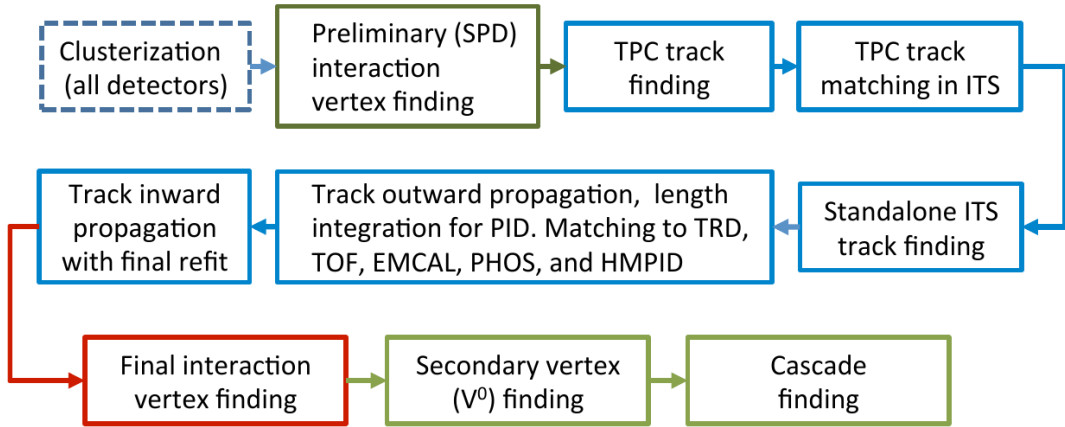


Figure 4.1: Event reconstruction scheme. Figure from [94].

closest approach (PCA) between two unlike-sign tracks is calculated. Once their PCA is obtained, the search for cascade decay can be initiated. The more detail information about central-barrel track reconstruction can be found in reference [94].

For the tracks used in this thesis, a set of track cuts requirements called GlobalSDD [15] is applied on Pb-Pb system. This track cuts require fitting result with $\chi^2/\text{ITS cluster} < 36$ and $\chi^2/\text{TPC cluster} < 4$. The tracks also need to hit at least 3 out of 6 ITS layers. And some of the hits must hit at least one SPD layer or the first SDD layer. Moreover, they must cross 70 pad rows out of 159 TPC's pad rows (there are 160 pad rows [72] but the innermost/outermost row does not give signal and only serves as voltage supplier). Also, the ratio between crossed rows and the readable clusters of the track is at least 80%. The tracks that come after secondary vertex are also rejected in the analysis because we want to observe correlation in the primary collision. The DCA of these tracks also must be close enough to primary vertex. Two sets of DCA criteria are set with respect to the beam axis (DCA_z) and its transverse plane (DCA_{xy}). It is required that $\text{DCA}_z < 2 \text{ cm}$ and $\text{DCA}_{xy} < 0.0105 \text{ cm} + 0.035 \text{ cm} \cdot \left(\frac{p_T}{\text{GeV}/c}\right)^{-1.1}$.

5 Analysis

The reconstructed tracks and the generated data from simulation need to be processed further with production code in order to produce the data used in this thesis. For this purpose, two-particle correlation method is used to construct jet fragmentation transverse momentum (j_T) distribution. The results are then saved into ROOT data file. The next step is processing the ROOT data file with analysis code. In this process, we extract j_T signals by subtracting combinatorial background from the raw j_T distribution. And finally, the Gaussian function is fitted to small j_T region that represents hadronization, and inverse gamma function is fitted to the rest of j_T region that represent parton showering. From there, we can study many things such as the width of j_T , yield-per-trigger particle, and how the centrality of collision and the presence of medium affect j_T . The following sections discuss the details of these operations.

5.1 Two-Particle Correlation

Two-particle correlation is a statistical method in which two particles' momenta from many events are paired [15]. In each event, leading or trigger particles within certain range of transverse momentum p_{Tt} are selected. Associated particles are picked up within the same event with condition that their momenta \vec{p}_a must be smaller than the momentum of the leading particle \vec{p}_t they are paired with. The associated particles also need to be in the same hemisphere with the leading particle so that $\vec{p}_t \cdot \vec{p}_a \geq 0$. The observable that is studied from pairing leading particle with associated particle is jet fragmentation transverse momentum j_T defined as:

$$j_T = \frac{|\vec{p}_t \times \vec{p}_a|}{|\vec{p}_t|}. \quad (5.1)$$

Many pairing in the same event and a lot of events provide enough statistic to generate j_T distributions. These distributions are assigned with three different binning categories. The first binning category is based on centrality d . The second binning category is based on $x_{||}$ defined by

$$x_{||} = \frac{\vec{p}_t \cdot \vec{p}_a}{\vec{p}_t^2}. \quad (5.2)$$

And the third binning category is the leading particle's transverse momentum p_{Tt} . For example, if we take a j_T distribution with $0 < d < 10\%$, $0.2 < x_{||} < 0.4$, and $8 < p_{Tt} < 10$ GeV/c categories, we only study the j_T distribution from events with centrality 0-10%, from any associated particle that fulfill the all prerequisites before with its \vec{p}_a must give $x_{||}$ value within the range 0.2-0.4, and from leading particle with p_{Tt} between 8 to 10 GeV/c.

Figure 5.1 illustrates why $x_{||}$ binning is chosen instead of associated particle transverse momentum (p_{Ta}) binning. If there are two associated particles with

momentum $\vec{p}_{a,1}$ and $\vec{p}_{a,2}$ that have same magnitude and opening angle with respect to \vec{p}_t but moving to different directions, they will give the same value of j_T but in different directions. Since $p_{Ta,1} > p_{Ta,2}$, random direction of j_T may cause undesired fluctuation between these two p_{Ta} -binning distributions. But with $x_{||}$ binning, j_T is filled to the same distribution regardless of its directions.

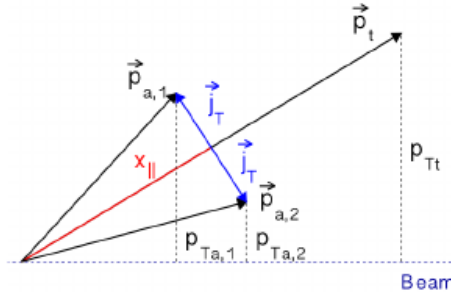


Figure 5.1: Illustration of why $x_{||}$ binning is chosen instead of p_{Ta} binning. Figure from [15].

When generating the j_T distributions, acceptance correction also need to be considered in order to make it comparable with the theory. This is because ALICE detector has limited acceptance about $-0.8 < \eta < 0.8$ and hence some particles beyond this acceptance limit begone undetected. This correction has been included in production code upon generating j_T distribution. More details about acceptance correction can be read in reference [15].

In generating background distributions, we assume that particles from the same jet are close to each other. Thus according to reference [15], pairs with large angular distance $\Delta\eta > 1$ are considered as background. To form a complete background distribution, we need to extrapolate these pairs to region $\Delta\eta < 1$. This is done by assigning new random $\Delta\eta$ values between zero and one 20 times to each pair with large $\Delta\eta$. Hence it gives a background estimation for the whole η range.

5.2 Signal Extraction

The following procedure is called η -gap method since the background distribution rely on the difference between pseudorapidities of the two-particles in each pair. A more varied method called R-gap method involves the difference between azimuthal angle $\Delta\phi$ and combined with $\Delta\eta$ variation into $R = \sqrt{\Delta\phi^2 + \Delta\eta^2}$. Reference [15] uses this method for pp and p-Pb systems to estimate systematic uncertainty by defining $R > 1$ as background. But since the elliptic and higher orders flow presences in Pb-Pb systems [96], we do not use R-gap method here due to large $\Delta\phi$ modulation.

The generated data, both background and j_T distributions, have distribution $\frac{1}{j_T} \frac{dN}{dj_T}$. In order to make them comparable with other data sets, scaling over number of trigger $\frac{1}{N_{trigg}}$ is applied on both distributions. To get the number of triggers N_{trigg} , we integrate over the trigger p_T distribution in certain range of d and p_{Tt} binning.

In order to extract the j_T signal, we can check first how the ratio of j_T distribution over background distribution behaves. The histogram division result is shown in Figure 5.2a. We can see there is a "hill" in the beginning of histogram; this is the signal that we want. As j_T grows, the ratio goes down and then tend to flat. But since the ratio is smaller than one, j_T signal will become negative if we subtract away the background directly without normalization. We need to scale the flat region to unity

by multiplying the background with normalization constant

$$r_s = \frac{\int_{n_{lb}}^{n_{bins}} \frac{1}{N_{trigg}} \frac{1}{j_T} \frac{dN}{dj_T} dj_T |_{j_T \text{ distribution}}}{\int_{n_{lb}}^{n_{bins}} \frac{1}{N_{trigg}} \frac{1}{j_T} \frac{dN}{dj_T} dj_T |_{Background}}. \quad (5.3)$$

The numerator is the integral of j_T distribution and the denominator is integral of background distribution. The integration is in the limit from lower bound value n_{lb} to the last bin n_{bins} of the histogram. In the data file, n_{bins} is set to 100. To find the n_{lb} , a constant number shown as red line in Figure 5.2a is fitted to a small region where the ratio start to be flat. This red line also acts as a ruler to our eyes. n_{lb} is the first bin whose ratio intersects or is below the red line at the start of flat region. After normalization, the flat region becomes unity like in Figure 5.2b and ready for background subtraction.

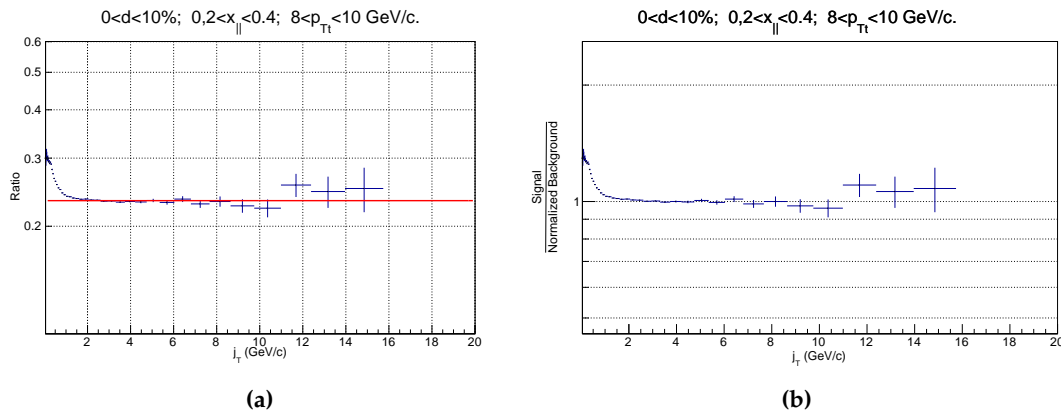


Figure 5.2: (a) The j_T distribution divided by background distribution. The hill above the red line is the wanted j_t signal. (b) The ratio after background normalization.

When j_T distribution is subtracted by the normalized background distribution, some bin contents become negative and are removed from histogram. Meanwhile some bin contents at large j_T still remain after background subtraction. It is plausible because j_T can be larger than p_{Tt} . But it has certain maximum limit for each p_{Tt} and $x_{||}$ binning. These limits are calculated in Appendix B. By setting up the maximum limit for each histogram, we discard any entries at j_T above the maximum value since they are not geometrically possible. Another explanation is that they arise from acceptance corrections during data production. At the edge of acceptance, the correlation can be very large and thus rise some false signals at large j_T . These contaminations can be removed by discarding entries less than 10 in j_T distribution (some exceptions may apply, see Appendix C) and removing very small entries after background subtraction. We can also do rebinning to rise the distribution so it give more statistic but at the cost of wider bin width because it merges two or more bins into one bin.

Figure 5.3 shows the comparison between unmodified signal and modified signal. In Figure 5.3a, a long tail is seen until $j_T = 20$ GeV/c. This is unphysical since the cut-off j_T limit for $8 < p_{Tt} < 10 < \text{GeV/c}$ binning calculated in Appendix B is about 13 GeV/c. Figure 5.3b is the result after discarding entries less than 10, remove any entries at bins above 13 GeV/c, and merging 2 bins. The modified signal in Figure 5.3b is much neater to fit with Gaussian and inverse gamma function explained in the next chapter.

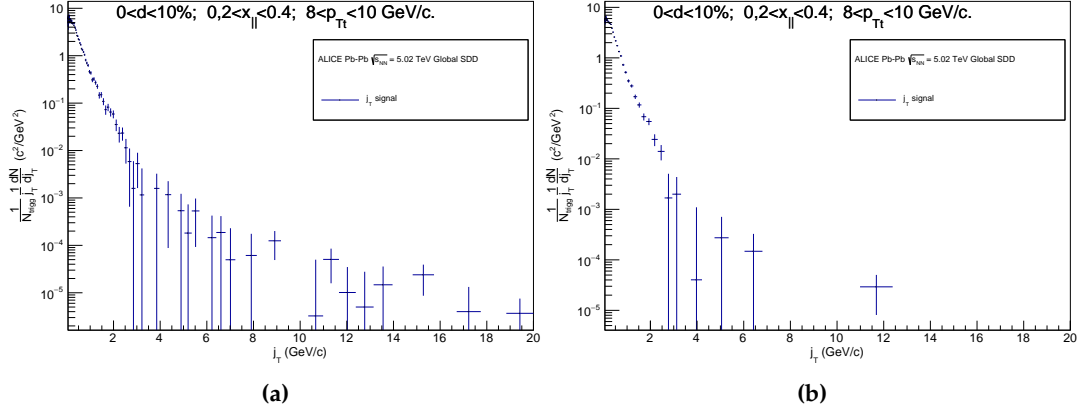


Figure 5.3: (a) The j_T signal without any modification. (b) The signal after discarding very small entries, setting cut-off limit, and rebinning.

5.3 Fitting j_T Signal

In reference [15], it has been established that hadronization occurs at small j_T region and larger j_T is generated during partonic evolution. Figure 5.4 shows the result from PYTHIA 8 [12] study in pp collision system. The initial state particles in this simulation study are two gluons. If the simulation is run without QCD showering, only hadronization that is simulated and hence, only red histogram appears from Figure 5.4. Since hadronization scheme in PYTHIA 8 follows the Lund string fragmentation model [13], the best function that fit the red histogram is a two-dimensional Gaussian function

$$f_G(j_T) = \frac{B_2}{B_1^2} e^{-\frac{j_T^2}{2B_1^2}}, \quad (5.4)$$

with B_1 and B_2 are free parameters for fitting the function. If QCD showering is involved in the simulation, black histogram appears in Figure 5.4, and produce long

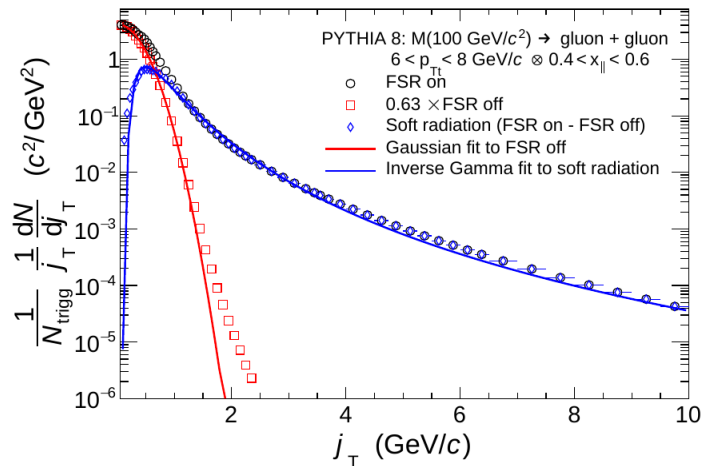


Figure 5.4: Fitting j_T signal from di-gluon PYTHIA study. When final state radiation (FSR) is turned on, the black histogram emerges. When FSR is turned off, there is no QCD showering so only red histogram appears. The blue histogram is obtained from subtracting the black histogram with the red histogram. Figure from [15].

tail. To find out the contribution from QCD showering, red histogram are scaled to the same height of black histogram at $j_T = 0$ before subtracting black histogram with red histogram. What is left after subtraction is the blue histogram in Figure 5.4. The function that fit well with the blue histogram is inverse gamma function

$$f_{IG}(j_T) = \frac{B_3 B_5^{B_4-1}}{\Gamma(B_4-1)} \frac{e^{-\frac{B_5}{j_T}}}{j_T^{B_4+1}} \quad (5.5)$$

with three free parameters B_3 , B_4 , and B_5 . It is necessary that $B_4 > 2$ in gamma function. Later on, the hadronization part is called narrow component while the QCD showering part is called wide component. The sum of them

$$\begin{aligned} f_{total}(j_T) &= f_G(j_T) + f_{IG}(j_T) \\ &= \frac{B_2}{B_1^2} e^{-\frac{j_T^2}{2B_1^2}} + \frac{B_3 B_5^{B_4-1}}{\Gamma(B_4-1)} \frac{e^{-\frac{B_5}{j_T}}}{j_T^{B_4+1}}. \end{aligned} \quad (5.6)$$

are called two-component function.

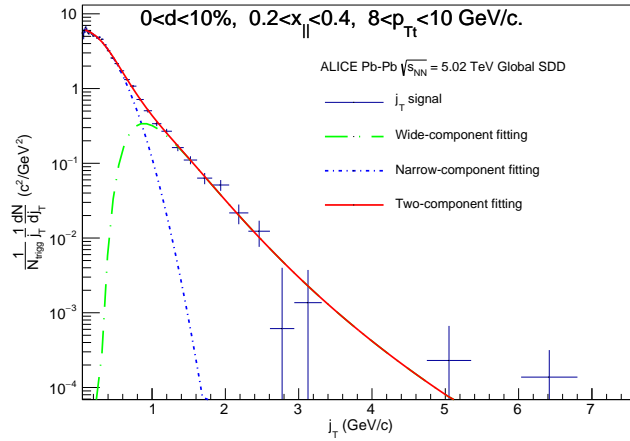


Figure 5.5: Fitting of j_T signal in Pb-Pb collision system. Fitting is done separately for both narrow and wide components before fitting them together as two-component.

The next step is to apply the results found in PYTHIA 8 study to Pb-Pb collision system. The final result of fitting for Pb-Pb system is shown in Figure 5.5. Since all the narrow, wide, and two-component functions fit well with j_T signal from Pb-Pb system, it shows that the study from PYTHIA 8 in pp collision is well established and applicable in general collision system. In the analysis code, narrow and wide components are fitted first separately to obtain the free parameters. The narrow component is fitted to low j_T and the wide component is fitted to high j_T . The parameters from the first fitting are then used in two-component function. Then the two-component function are then fitted again to the whole j_T signal to refine the parameters' values. The final values of these parameters are set again to the narrow and wide components. These repetitive fittings lead to a better convergence of the multi-parameter fit.

5.4 Finding the RMS of j_T and yield per trigger particles

The purpose of fitting j_T signal is to find the root mean square (RMS) of j_T and yield-per-trigger particles. From reference [15], the yield per trigger for narrow component is

$$\frac{\mathcal{Y}_G}{N_{trigg}} = \int_{-\infty}^{\infty} j_T \frac{B_2}{B_1^2} e^{-\frac{j_T^2}{2B_1^2}} dj_T = B_2. \quad (5.7)$$

And for wide component, the yield per trigger is

$$\frac{\mathcal{Y}_{IG}}{N_{trigg}} = \int_{-\infty}^{\infty} j_T \frac{B_3 B_5^{B_4-1}}{\Gamma(B_4-1)} \frac{e^{-\frac{B_5}{j_T}}}{j_T^{B_4+1}} dj_T = B_3. \quad (5.8)$$

The RMS of j_T for narrow component is given by

$$\sqrt{\langle j_T^2 \rangle_G} = \left(\frac{1}{B_2} \int_0^{\infty} j_T^3 \frac{B_2}{B_1^2} e^{-\frac{j_T^2}{2B_1^2}} dj_T \right)^{\frac{1}{2}} = \sqrt{2} B_1. \quad (5.9)$$

And for wide component, we get

$$\sqrt{\langle j_T^2 \rangle_{IG}} = \left(\frac{1}{B_3} \int_0^{\infty} j_T^3 \frac{B_3 B_5^{B_4-1}}{\Gamma(B_4-1)} \frac{e^{-\frac{B_5}{j_T}}}{j_T^{B_4+1}} dj_T \right)^{\frac{1}{2}} = \frac{B_5}{\sqrt{(B_4-2)(B_4-3)}}. \quad (5.10)$$

It is required that $B_4 > 3$ for both the initial parameter setting and the final fit result. Once the fitting has been done and all final parameters values are obtained, it is straightforward to plug them into the above equations. The statistical errors for RMS and yield are taken from their parameters' fitting error and squared summed up in

$$\Delta f(x_1, \dots, x_n) = \sqrt{\sum_{i=1}^n \left(\frac{\partial f}{\partial x_i} \Delta x_i \right)^2}.$$

5.5 Comparison Between Different Centrality And Different Collision System

Once we have j_T signals in hand, we can compare them to each other. The area of interest here is to explore how the presence of medium affect j_T in various p_{Tt} and $x_{||}$ binning. Let us define the R_{AA} -like ratio called "intercentrality" ratio

$$R_C = \frac{C_{central}}{C_{peripheral, pp, \text{ or } p-Pb}} = \frac{\frac{1}{N_{trigg}} \frac{dN}{j_T dj_T} \Big|_{central}}{\frac{1}{N_{trigg}} \frac{dN}{j_T dj_T} \Big|_{peripheral, pp, \text{ or } p-Pb}}. \quad (5.11)$$

The numerator $C_{central}$ in equation 5.11 is the j_T signal from central collision, and the denominator $C_{peripheral, pp, \text{ or } p-Pb}$ is the j_T signal from peripheral collision or another collision system.

6 Results

6.1 Results for RMS of j_T and Yield per Trigger Particle

After the fitting has been done, the results for $\sqrt{\langle j_T^2 \rangle}$ and yield per trigger particle are obtained and shown in Figures 6.1 and 6.2. Each fitting result to j_T signal in all p_{Tt} , $x_{||}$, and centrality bins for Pb-Pb ALICE experiment data can be found in Appendix

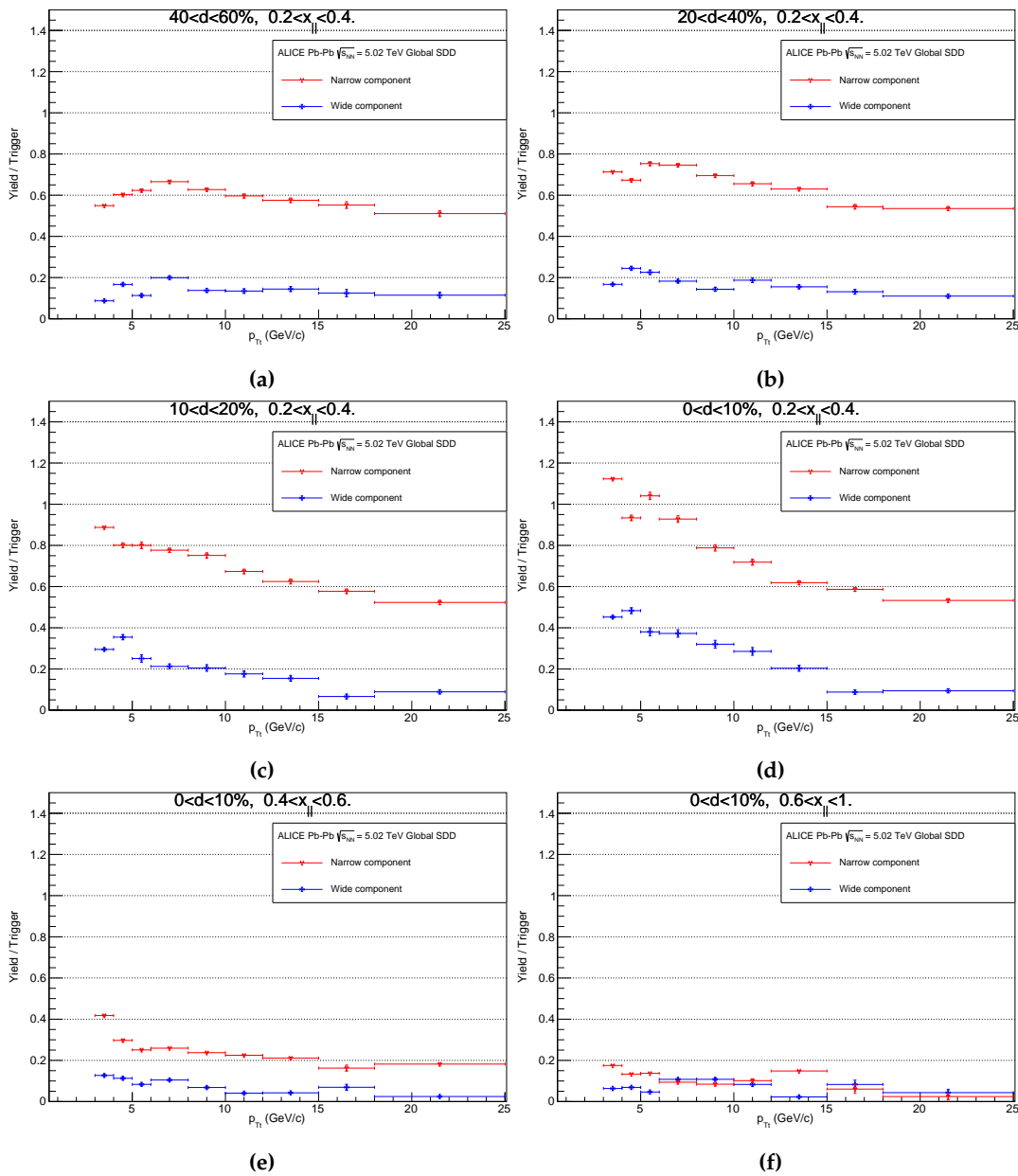


Figure 6.1: Yield/trigger particle from j_t signals.

C. Through Figures 6.1a, 6.1b, 6.1c, and 6.1d, we can see how the trend in yield per trigger particle for both narrow and wide components change as centrality classes switch from peripheral to central collision. As we expect from high-multiplicity environment, the yield-per-trigger trend increases as the collisions become more central. But the increasing trend is only significant at lower p_{Tt} bins. This indicates that the presence of medium suppresses high- p_T particle production. The suppression happens because jets lose their energy while traversing inside medium and thus enhance further particle yield at lower p_{Tt} bins. On the other hand, through the Figures 6.1d, 6.1e, and 6.1f, we see a decreasing trend over $x_{||}$ bins in yield per trigger particle for both wide and narrow components. The similar decreasing trend over $x_{||}$ bins is also produced in references [15, 16] both for pp and p-Pb data but at lower value since those systems produce less particles. This is understandable since high- p_T particle become rarer while p_{Tt} also increases when $x_{||}$ increases. Thus the trigger

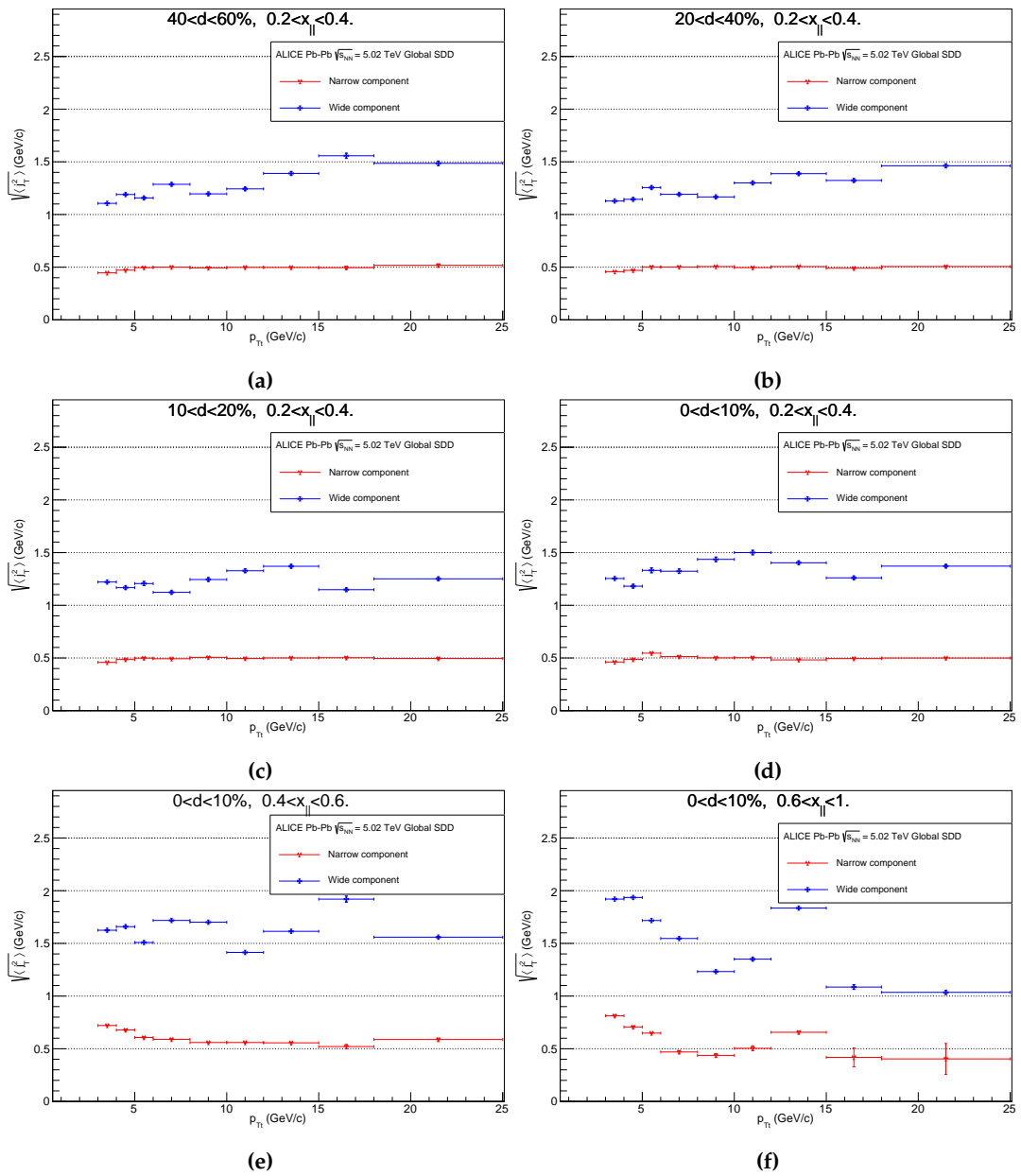


Figure 6.2: RMS of j_T signals.

particle find less pairs at large $x_{||}$.

Meanwhile in the results for RMS of j_T , there are certain fluctuations over p_{Tt} bins in wide component. Currently there is no known reason behind these fluctuations. It can be that the actual error is larger than the statistical error bar since we have not determined the systematic uncertainty for this analysis. For the narrow component, we can see the flat trend between p_{Tt} bins in Figures 6.2a, 6.2b, 6.2c, and 6.2d. The value for RMS of j_T is about 0.5 GeV/c within $0.2 < x_{||} < 0.4$ bin regardless of centrality classes. This suggest that $\sqrt{\langle j_T^2 \rangle}$ for hadronization is unaffected by the presence of medium.

6.2 Comparison To pp Data

Figures 6.1a-d and 6.2a-d can be stacked in the same canvas along with pp data like in Figures 6.3. On the left column, Pb-Pb data is compared to pp $\sqrt{s} = 5.02$ TeV. And on the right column it is compared to pp $\sqrt{s} = 7$ TeV data from references [15, 16]. In pp $\sqrt{s} = 7$ TeV data, we run out of statistic at $p_{Tt} > 15$ GeV/c. Through Figure 6.3a and 6.3b, we can see the contrast between different centrality classes and pp system due to high-multiplicity environment and medium modification as explained before. For the wide component yield per trigger particle, there are slightly rising trends as a

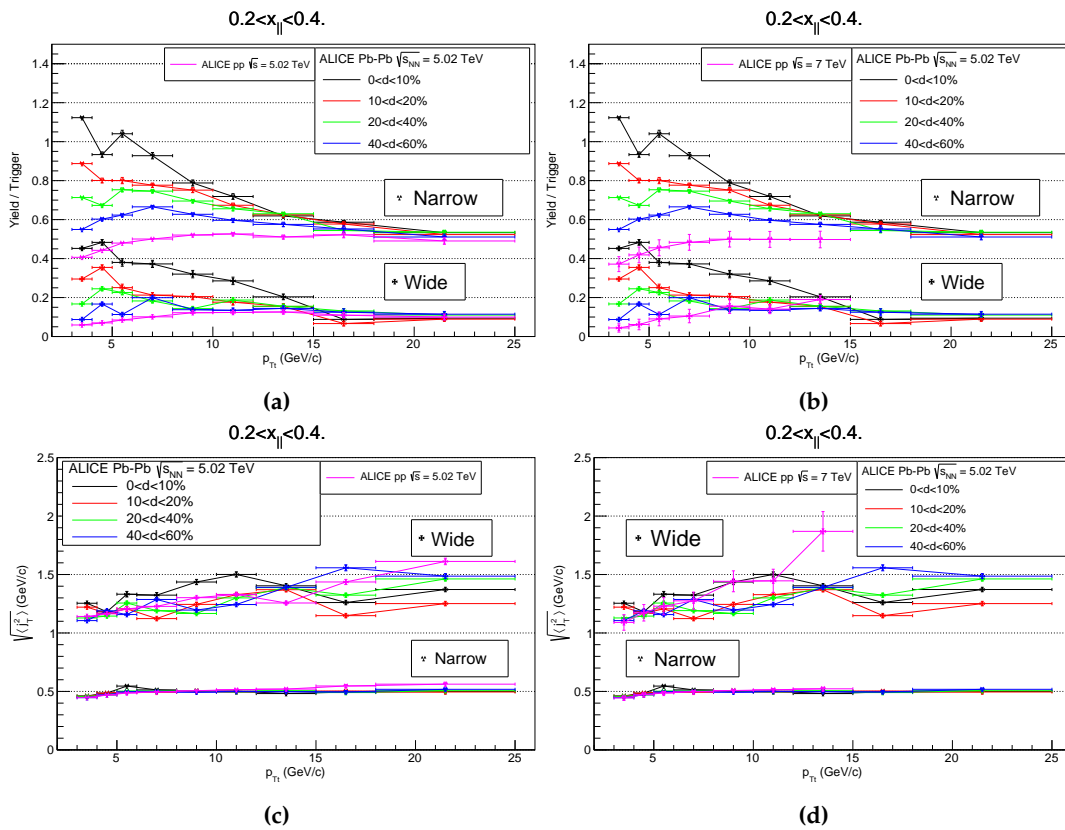
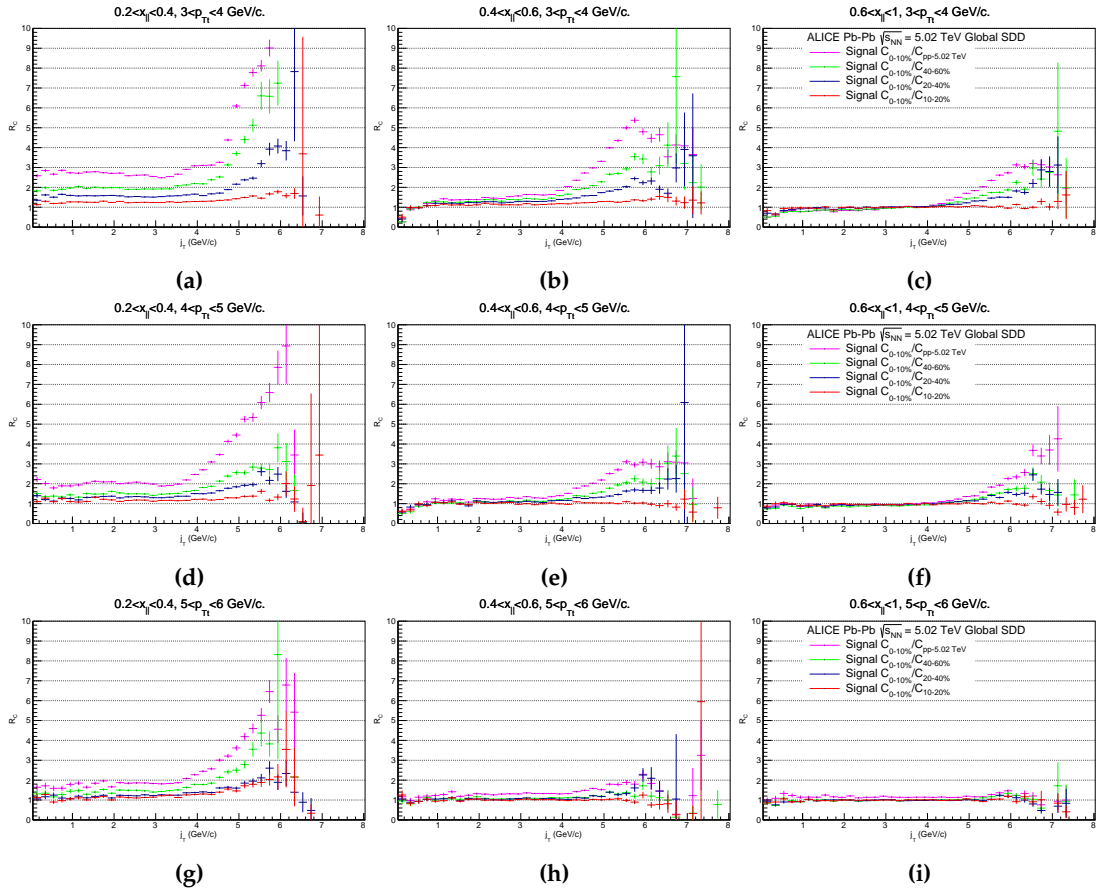


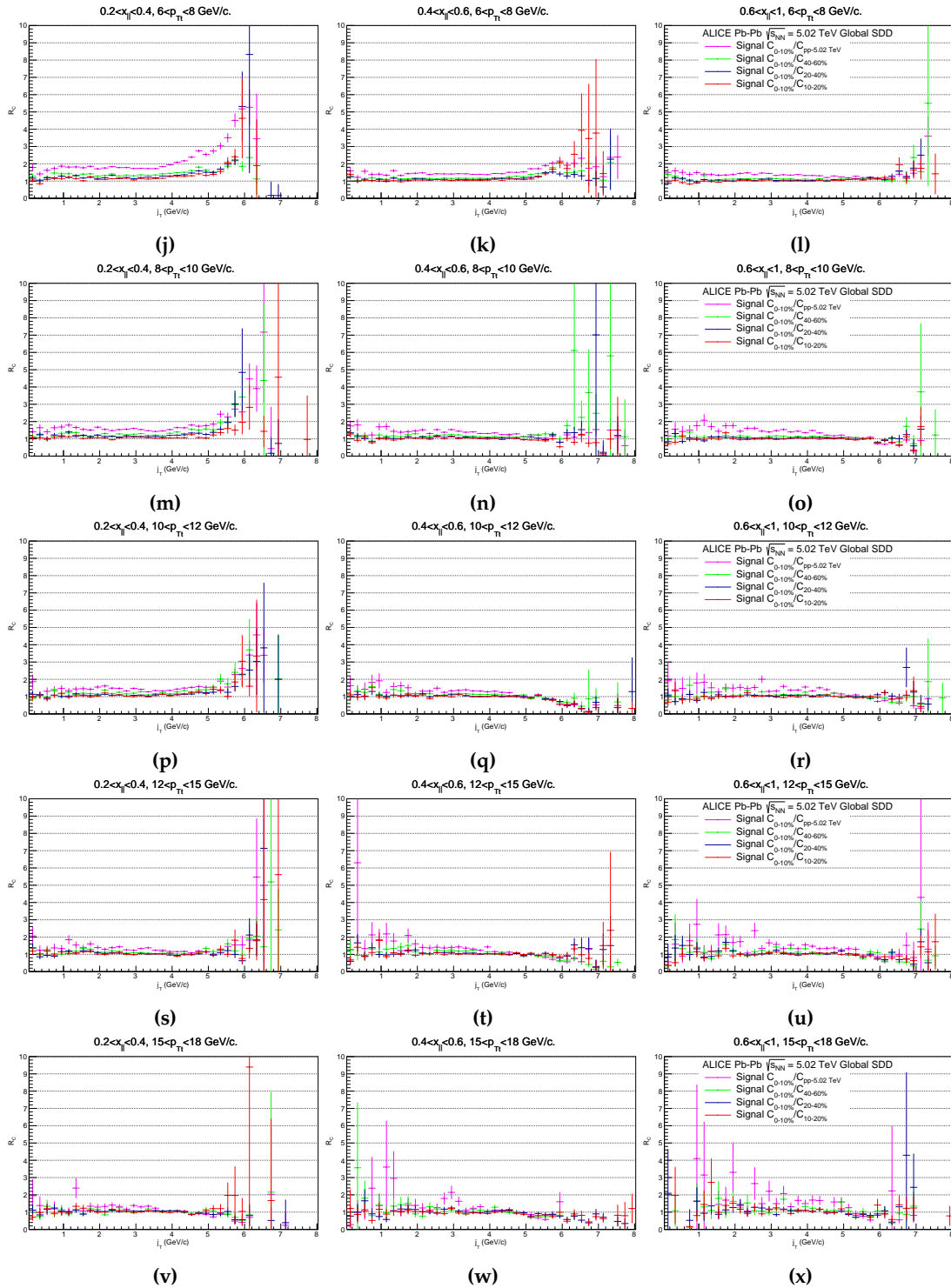
Figure 6.3: Comparison of yield/trigger ((a), (b)) and $\sqrt{\langle j_T^2 \rangle}$ ((c), (d)) between different centrality classes and pp system.

function of p_{Tt} in both pp 5.02 TeV and 7 TeV due to the increasing phase space left for pQCD splittings [15]. But in Pb-Pb system, the medium modification and high multiplicity due to large N_{coll} override this effect, causing the particle production

enhancement at lower p_{Tt} . For the narrow component RMS of j_T in $0.2 < x_{||} < 0.4$ bin, Figures 6.3c and 6.3d show that all centrality classes and pp system nearly overlap with each other, suggesting that $\sqrt{\langle j_T^2 \rangle}$ for hadronization is also system and energy independent. For wide component RMS of j_T , we don't see any fluctuation in pp system like in Pb-Pb system.

In Figure 6.4, the collection of intercentrality ratios along with central Pb-Pb to pp j_T signal ratio are presented. The $18 < p_{Tt} < 25$ bin is not presented since we run out of statistic in ALICE pp $\sqrt{s} = 5.02$ TeV data at $0.6 < x_{||} < 1$ bin. At small p_{Tt} bins, there are clear separations of R_C between different centrality classes and pp due to different multiplicity in the systems. But the gaps start to emerge into unity as p_{Tt} bins grow. This suggests that j_T at lower p_{Tt} bins receive a contribution from high- p_T partons that loss their energy inside medium. At low p_{Tt} , we see the growths in R_C at large j_T and these growths depend on centrality and collision system. The growths start weak in $0 < d < 10\%$ over $20 < d < 40\%$ signal ratio and become stronger as we compare the central collision to peripheral collision. And finally, the stronger j_T growths is seen in central Pb-Pb over pp system. The j_T growths suggest the broadening angle in jets that loss their energy. But the broadening angle diminishes at high p_{Tt} bins, suggesting that high energy partons either survive during their evolution in medium or are produced at the edge of QGP fireball and move to outside. These results along with the yield per trigger particle results confirm the enhancement of low p_T particle production due to jet energy loss in medium.



Figure 6.4: Intercentricity ratio R_C of j_T signals.

6.3 Comparison To AMPT 2 Model

Figures 6.5 and 6.6 show the comparison between ALICE experiment data and AMPT 2 model. For yield per trigger particle, AMPT 2 simulation overestimates particle production at $3 < p_{Tt} < 6$ and $0.2 < x_{||} < 0.4$ regions. Thus HIJING 1.383 need certain tuning for this energy scale since AMPT 2 follows minijet parton production from this HIJING version [47]. But at higher p_{Tt} bins, AMPT 2 follows

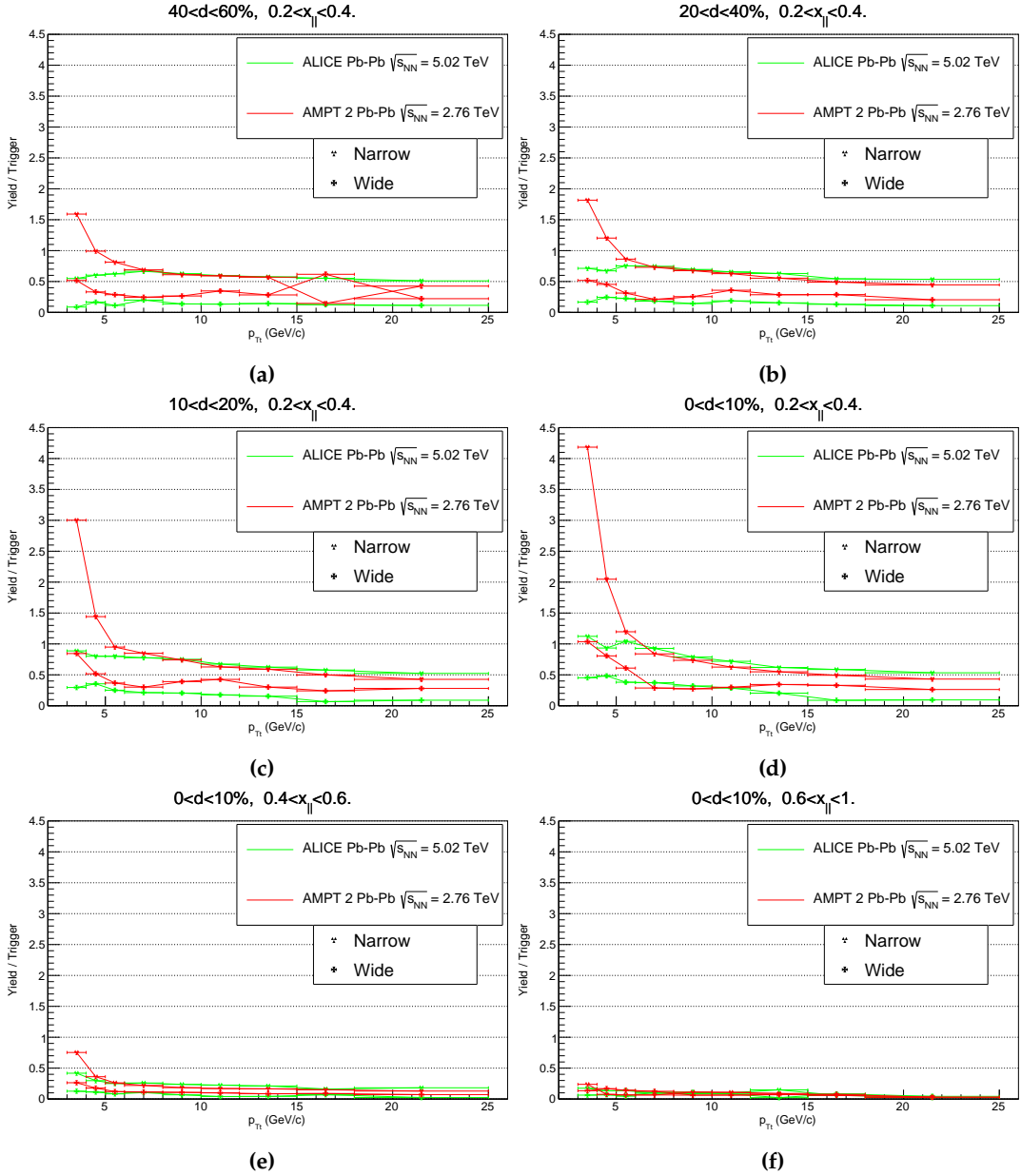


Figure 6.5: Comparison of yield/trigger between ALICE data and AMPT simulation.

the same trend as ALICE experiment results and even overlap at several points. But at central collisions, the wide component yield per trigger from AMPT 2 slightly overestimate particle production at high p_{Tt} . It implies that the jet energy loss is slightly harder than ZPC model, limiting the production of high- p_T associated particles to pair with the leading particle. Another possibility is that beside ZPC cascade, partons also lose their energy by radiating soft gluon. And this is not taken into account in AMPT model.

For RMS of j_T , the narrow component results for both ALICE experiment and AMPT 2 are quite in agreement. Meanwhile for the wide component, the RMS of j_T results for AMPT 2 slightly overestimate most of the ALICE experiment data points. But we also see the similar fluctuations over p_{Tt} in AMPT 2 results. This increase the necessity to study the systematic uncertainty to find out whether the resulting error

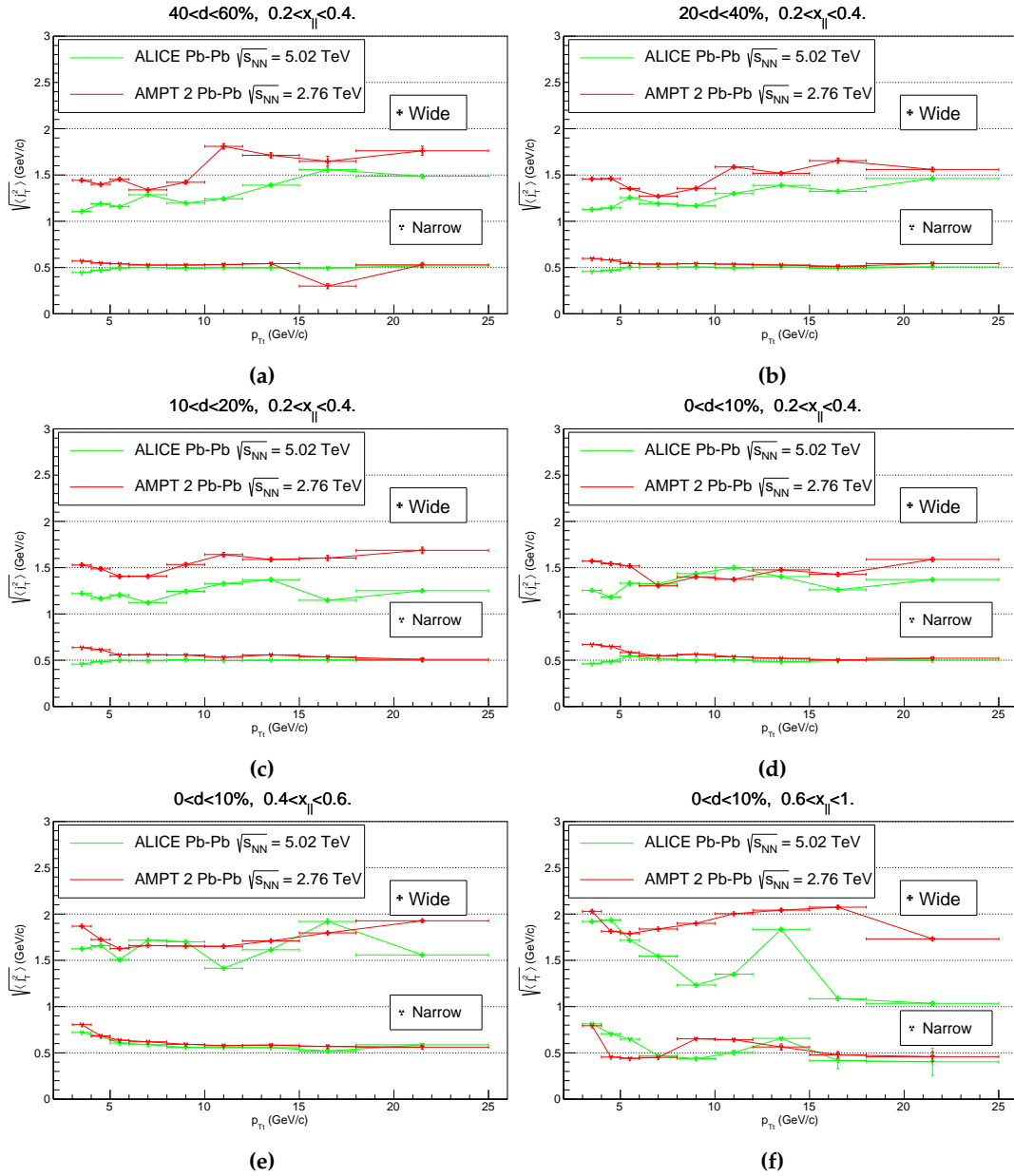


Figure 6.6: Comparison of $\sqrt{\langle j_T^2 \rangle}$ between ALICE data and AMPT simulation.

bar overlap to each other or not. If later the fluctuations still persist outside the error bar ranges, then one may need to look after why such fluctuations occur.

7 Conclusions And Insights

The jet-fragmentation transverse momentum (j_T) in Pb-Pb $\sqrt{s_{NN}} = 5.02$ TeV is studied with two-particle correlation. This thesis is the continuation from study of jet-fragmentation transverse momentum in pp and p-Pb collision systems [15, 16]. The similar Gaussian distribution (narrow component) for hadronization and inverse gamma distribution (wide component) for QCD splitting are also observed in Pb-Pb system. The results from Pb-Pb system are then compared to pp system and AMPT 2 simulation.

The results for yield per trigger from Pb-Pb, both for narrow and wide components, show a rising trend of lower p_{Tt} bins as collision become more central due to high-multiplicity environment and medium modification. Higher- p_T partons loss their energy to medium and thus contribute to the particle production at lower p_{Tt} bin instead. Therefore these results provide evidence to jet quenching. This conclusion is also supported by the contrast to the lower yield per trigger in pp system which is lack of the bulk of QGP medium. In comparison to AMPT 2 simulation, the minijet parton production in HIJING 1.383 which is used in AMPT 2 overestimates low- p_T particle production at $3 < p_{Tt} < 6$ Gev/c and $0.2 < x_{||} < 0.4$ regions, suggesting that this model need certain tuning with the up-to-date data.

The $\sqrt{\langle j_T^2 \rangle}$ results for narrow component suggest that hadronization is independent of centrality and collision system. Thus these results answer the previous study [15] that hadronization happens outside the hot medium. On the other hand, the $\sqrt{\langle j_T^2 \rangle}$ results shows a clear fluctuation over p_{Tt} and dependency with different collision system, centrality classes, and $x_{||}$ categories. However, the actual error bar can be larger than that from statistical error.

The error bar in this thesis's results are generated only from statistical error and very small. Thus the study to estimate the systematic error becomes important for future study. The relation between collective flow to j_T , if any, is also interesting to be investigated. In AMPT 2, cross section formula for gluon-gluon scattering in ZPC model is also applied to (anti)quark-(anti)quark and (anti)quark-gluon [51, 89]. It would be better if the cross section formula for each type of parton scattering is used. Furthermore, comparison with other Monte-Carlo simulations like Jet Evolution With Energy Loss (JEWEL) [97], HIJING++ [98], and Yet another Jet Energy loss Model (YaJEM) [99] are interesting to explore.

Bibliography

- [1] R. K. Ellis, B. R. Webber, and W. J. Stirling, "QCD and Collider Physics.", Cambridge University Press, 1996.
- [2] W. Busza, K. Rajagopal, W. V. D. Schee, "Heavy Ion Collisions: The Big Picture and the Big Questions", Annu. Rev. Nucl. Part. Sci. 2018. 68:339–76.
<https://www.annualreviews.org/doi/abs/10.1146/annurev-nucl-101917-020852>
- [3] D. Gorbunov, and V. Rubakov, *Introduction to The Theory of The Early Universe, Hot Big Bang Theory*, World Scientific Publishing Co. Pte. Ltd., 2011.
- [4] U. Heinz and R. Snellings, "Collective Flow and Viscosity in Relativistic Heavy-Ion Collisions", Annu. Rev. Nucl. Part. Sci. 2013. 63:123–51.
<https://www.annualreviews.org/doi/pdf/10.1146/annurev-nucl-102212-170540>
- [5] J. D. Bjorken, "Energy Loss of Energetic Partons in Quark-Gluon Plasma: Possible Extinction of High p_T Jets in Hadron-Hadron Collisions", FERMILAB-Pub-82/59-THY, 1982.
<https://lss.fnal.gov/archive/1982/pub/Pub-82-059-T.pdf>
- [6] STAR Collaboration, "Direct observation of dijets in central Au+Au collisions at $\sqrt{s_{NN}} = 200$ GeV", Phys. Rev. Lett. 97 (2006) 162301.
<https://arxiv.org/abs/nucl-ex/0604018>
- [7] PHENIX Collaboration, "Transverse momentum and centrality dependence of dihadron correlations in Au+Au collisions at $\sqrt{s_{NN}} = 200$ GeV: Jet-quenching and the response of partonic matter", Phys. Rev. C 77 (2008) 011901.
<https://arxiv.org/abs/0705.3238>
- [8] ATLAS Collaboration, "Observation of a centrality-dependent dijet asymmetry in lead-lead collisions at $\sqrt{s_{NN}} = 2.76$ TeV with the ATLAS detector at the LHC", Phys. Rev. Lett. 105 (2010) 252303.
<http://www.arxiv.org/abs/1011.6182>
- [9] CMS Collaboration, "Observation and studies of jet quenching in PbPb collisions at $\sqrt{s_{NN}} = 2.76$ TeV", Phys. Rev. C 84 (2011) 024906.
<https://arxiv.org/abs/1102.1957>
- [10] CMS Collaboration, "Jet momentum dependence of jet quenching in PbPb collisions at $\sqrt{s_{NN}} = 2.76$ TeV", Phys. Lett. B 712 (2012) 176.
<http://www.arxiv.org/abs/1202.5022>
- [11] ALICE Collaboration, "Measurement of jet suppression in central Pb-Pb collisions at $\sqrt{s_{NN}} = 2.76$ TeV", Phys. Lett. B 746 (2015) 1.
<http://www.arxiv.org/abs/1502.01689>

- [12] T. Sjöstrand et al., "An Introduction to PYTHIA 8.2", CERN-PH-TH-2014-190.
<https://arxiv.org/abs/1410.3012>
- [13] B. Andersson, G. Gustafson, G. Ingelman, and T. Sjöstrand, *Parton Fragmentation and String Dynamics*, Phys.Rept. 97 (1983) 31–145.
<https://www.sciencedirect.com/science/article/abs/pii/S0370157383900807>
- [14] P. Štefko, "Study of jet quenching in heavy ion collisions at LHC using ATLAS detector", 18th Conference of Czech and Slovak Physicists, 2014. https://www.researchgate.net/figure/Sketch-of-the-jet-quenching-mechanism-during-heavy-ion-collision_fig75_277669564
- [15] J. Viinikainen, *Jet Fragmentation Transverse Momentum from h-h Correlations In p-p and p-Pb Collisions*, University of Jyväskylä, 2017.
<https://jyx.jyu.fi/handle/123456789/56142>
- [16] ALICE Collaboration, S. Acharya et al., *Jet Fragmentation Transverse Momentum from di-hadron correlations in $\sqrt{s} = 7$ TeV pp and $\sqrt{s_{NN}} = 5.02$ TeV p-Pb collisions*", JHEP 1903 (2019) 169.
<https://arxiv.org/abs/1811.09742>
- [17] B. Zhang, "Multiphase transport model for relativistic nuclear collisions", et al, Phys. Rev.C61, 067901, 2000.
<https://journals.aps.org/prc/abstract/10.1103/PhysRevC.61.067901>
- [18] Z.W. Lin, et al, "Partonic Effects in Heavy Ion Collisions at RHIC", Phys. Rev. C64, 011902, 2001.
<https://arxiv.org/pdf/nucl-th/0205056.pdf>
- [19] Z.W. Lin, et al., "A Multi-Phase Transport Model for Relativistic Heavy Ion Collisions", Phys. Rev. C72, 064901, 2005.
<https://arxiv.org/abs/nucl-th/0411110>
- [20] Z.W. Lin, "Evolution of transverse flow and effective temperatures in the parton phase from a multiphase transport model", Phys. Rev. C90, 014904 (2014).
<https://journals.aps.org/prc/abstract/10.1103/PhysRevC.90.014904>
- [21] B. Nachmana and M. L. Manganob, "Observables for possible QGP signatures in central pp collisions", Eur. Phys. J. C 78 (2018) 343.
<https://arxiv.org/abs/1708.08369>
- [22] K. Tywoniuk, "Is there jet quenching in pPb?", Nuclear Physics A 926 (2014) 85–91.
<https://www.sciencedirect.com/science/article/pii/S0375947414001055>
- [23] T. Renk, "Jet correlations - opportunities and pitfalls", Nucl. Phys. A932 (2014) 334–341.
<https://arxiv.org/abs/1404.0793>
- [24] T. Renk and K. J. Eskola, "Hard dihadron correlations in heavy-ion collisions at RHIC and LHC", Phys. Rev. C84 (2011) 054913.
[urlhttps://arxiv.org/abs/1106.1740](https://arxiv.org/abs/1106.1740)

- [25] V. N. Gribov and L. N. Lipatov, "Deep inelastic $e p$ scattering in perturbation theory", Sov. J. Nucl. Phys. 15 (1972) 438–450. [Yad. Fiz.15,781(1972)].
- [26] G. Altarelli and G. Parisi, "Asymptotic Freedom in Parton Language", Nucl. Phys. B126 (1977) 298–318.
<https://www.sciencedirect.com/science/article/pii/0550321377903844>
- [27] Y. L. Dokshitzer, "Calculation of the Structure Functions for Deep Inelastic Scattering and $e^+ e^-$ Annihilation by Perturbation Theory in Quantum Chromodynamics", Sov. Phys. JETP 46 (1977) 641–653. [Zh. Eksp. Teor. Fiz.73,1216(1977)].
- [28] G. Dissertori, "The Determination of the Strong Coupling Constant", arXiv:1506.05407v1, hep-ex, 2015.
<https://arxiv.org/pdf/1506.05407.pdf>
- [29] V. V. Sudakov, "Vertex parts at very high-energies in quantum electrodynamics", Sov. Phys. JETP 3 (1956) 65–71. [Zh. Eksp. Teor. Fiz.30,87(1956)].
- [30] Y. L. Dokshitzer, V. A. Khoze, A. H. Müller, and S. I. Troian, "Basics of Perturbative QCD", Editions Frontières, Gif-sur-Yvette, France, 1991.
- [31] A. Buckley et al., "General-purpose event generators for LHC physics", Phys. Rept. 504 (2011) 145–233.
<https://arxiv.org/abs/1101.2599>
- [32] T. S. Biro, P. Levai and J. Zimanyi, "ALCOR: a dynamical model for hadronization", Phys. Lett. B 347, 6-12, 1995.
<https://www.sciencedirect.com/science/article/pii/037026939500029K>
- [33] T. S. Biro, "Quark Coalescence and Hadronic Equilibrium", arXiv:hep-ph/0005067, 2000.
<https://arxiv.org/abs/hep-ph/0005067>
- [34] J. Zimanyi, T. S. Biro, T. Csorgo and P. Levai, "Quark liberation and coalescence at CERN SPS", Phys. Lett. B 472, 243-246, 2000.
<https://arxiv.org/abs/hep-ph/9904501>
- [35] J. Zimanyi, P. Levai, T. Csorgo and T. S. Biro, "Hyperon ratios at RHIC and the coalescence predictions at mid-rapidity", arXiv:hep-ph/0103156, 2001.
<https://arxiv.org/abs/hep-ph/0103156>
- [36] ALICE Collaboration, B. Abelev et al. "Centrality determination of Pb-Pb collisions at $\sqrt{s_{NN}} = 2.76$ TeV with ALICE", Phys.Rev. C88.4, 2013.
arxiv.org/abs/1301.4361
- [37] M. Miller, K. Reygers, S. J. Sanders, and P. Steinberg, "Glauber Modeling in High Energy Nuclear Collisions", Ann. Rev. Nucl. Part. Sci. 57, 205, 2007.
<https://arxiv.org/abs/nucl-ex/0701025>
- [38] R. Snellings, "Elliptic flow: a brief review", New J.Phys. 13 (2011) 055008.
<https://iopscience.iop.org/article/10.1088/1367-2630/13/5/055008>

- [39] A. Bzdak et al., "Mapping the Phases of Quantum Chromodynamics with Beam Energy Scan", arXiv:1906.00936 [nucl-th], 2019.
<https://arxiv.org/abs/1906.00936>
- [40] ALICE Collaboration, K. Aamodt et al., "Higher harmonic anisotropic flow measurements of charged particles in Pb-Pb collisions at $\sqrt{s_{NN}} = 2.76$ TeV", Phys. Rev. Lett. 107 (2011) 032301.
<https://arxiv.org/abs/1105.3865>
- [41] J. Parkkila, "Measuring the non-linear hydrodynamic response of higher flow harmonics in Pb-Pb at $\sqrt{s_{NN}} = 2.76$ TeV", University of Jyväskylä, 2017.
<https://jyx.jyu.fi/handle/123456789/54941>
- [42] PHENIX Collaboration, K. Adcox et al., "Suppression of hadrons with large transverse momentum in central Au+Au collisions at $\sqrt{s_{NN}} = 130$ GeV", Phys. Rev. Lett. 88 (2002) 022301.
<https://arxiv.org/abs/nucl-ex/0109003>
- [43] STAR Collaboration, J. Adams et al., "Experimental and theoretical challenges in the search for the quark gluon plasma: The STAR Collaboration's critical assessment of the evidence from RHIC collisions", Nucl. Phys. A757 (2005) 102–183.
<https://arxiv.org/abs/nucl-ex/0501009>
- [44] PHENIX Collaboration, K. Adcox et al., "Formation of dense partonic matter in relativistic nucleus-nucleus collisions at RHIC: Experimental evaluation by the PHENIX collaboration", Nucl. Phys. A757 (2005) 184–283.
<https://arxiv.org/abs/nucl-ex/0410003>
- [45] ALICE Collaboration, K. Aamodt et al., "Suppression of Charged Particle Production at Large Transverse Momentum in Central Pb-Pb Collisions at $\sqrt{s_{NN}} = 2.76$ TeV", Phys. Lett. B696 (2011) 30–39.
<https://arxiv.org/abs/1012.1004>
- [46] ATLAS Collaboration, G. Aad et al., "Observation of a Centrality-Dependent Dijet Asymmetry in Lead-Lead Collisions at $\sqrt{s_{NN}} = 2.76$ TeV with the ATLAS Detector at the LHC", Phys.Rev.Lett.105:252303, 2010.
<https://arxiv.org/abs/1011.6182>
- [47] X. N. Wang, "Role of multiple minijets in high-energy hadronic reactions", Phys. Rev. D 43, 104, 1991.
<https://journals.aps.org/prd/abstract/10.1103/PhysRevD.43.104>
- [48] X. N. Wang and M. Gyulassy, "HIJING: A Monte Carlo model for multiple jet production in pp, pA, and AA collisions", Phys. Rev. D 44, 3501, 1991.
<https://journals.aps.org/prd/abstract/10.1103/PhysRevD.44.3501>
- [49] X. N. Wang and M. Gyulassy, "Systematic study of particle production in p + p(\bar{p}) collisions via the HIJING model", Phys. Rev. D 45, 844, 1992.
<https://journals.aps.org/prd/abstract/10.1103/PhysRevD.45.844>
- [50] M. Gyulassy and X. N. Wang, "HIJING 1.0: A Monte Carlo Program for Parton and Particle Production in High Energy Hadronic and Nuclear Collisions", Comput. Phys. Commun. 83, 307, 1994.
<https://arxiv.org/abs/nucl-th/9502021>

- [51] B. Zhang, "ZPC 1.0.1: a parton cascade for ultrarelativistic heavy ion collisions", *Comput. Phys. Commun.* 109, 193, 1998.
<https://arxiv.org/abs/nucl-th/9709009>
- [52] CERN's web, "09 December 1949 Origins", <https://timeline.web.cern.ch/origins>, accessed on 16 January 2020.
- [53] CERN's web, "Our History", <https://home.cern/about/who-we-are/our-history>, accessed on 16 January 2020.
- [54] CERN's web, "Our Missions", <https://home.cern/about/who-we-are/our-mission>, accessed on 16 January 2020.
- [55] CERN's accelerators complex map, cds.cern.ch/record/2684277, accessed on 16 January 2020, ©2019, CERN.
- [56] A. Beuret *et al.*, "The LHC Lead Injector Chain", Proceedings of EPAC 2004, Lucerne, Switzerland.
<http://accelconf.web.cern.ch/AccelConf/e04/PAPERS/TUPLT011.PDF>
- [57] C. Carli, D. Hatzifotiadou, "Where do lead ion beams come from?", <http://alicematters.web.cern.ch/?q=lead-ion-beam-origins>, 17 November 2010, accessed on 17 January 2020.
- [58] D. Manglunki, "Recent Beam Performance Achievements With The Pb-Ion Beam In SPS for LHC Physics Run", 10th Int. Particle Accelerator Conf., 2019.
<http://accelconf.web.cern.ch/AccelConf/ipac2019/papers/mopgw069.pdf>
- [59] L. Evans, P. Bryant, "LHC Machine", *JINST* 3 (2008) S08001.
<https://iopscience.iop.org/article/10.1088/1748-0221/3/08/S08001/meta>
- [60] CERN Document Server, "Pulling together: Superconducting electromagnets", <https://cds.cern.ch/record/1997395?ln=en>, accessed on 27 January 2020.
- [61] ATLAS Collaboration, G. Aad *et al.*, "The ATLAS Experiment at the CERN Large Hadron Collider", *JINST* 3 (2008) S08003.
<https://iopscience.iop.org/article/10.1088/1748-0221/3/08/S08003>
- [62] ALICE Collaboration, K. Aamodt *et al.*, "The ALICE experiment at the CERN LHC", *JINST* 3 (2008) S08002.
<https://iopscience.iop.org/article/10.1088/1748-0221/3/08/S08002>
- [63] CMS Collaboration, S. Chatrchyan *et al.*, "The CMS Experiment at the CERN LHC", *JINST* 3 (2008) S08004.
<https://iopscience.iop.org/article/10.1088/1748-0221/3/08/S08004>
- [64] TOTEM Collaboration, G. Anelli *et al.*, "The TOTEM experiment at the CERN Large Hadron Collider" *JINST* 3 (2008) S08007.
<https://iopscience.iop.org/article/10.1088/1748-0221/3/08/S08007>
- [65] LHCb Collaboration, A. A. Alves, Jr. *et al.*, "The LHCb Detector at the LHC", *JINST* 3 (2008) S08005.
<https://iopscience.iop.org/article/10.1088/1748-0221/3/08/S08005>

- [66] LHCf Collaboration, O. Adriani et al., "*The LHCf detector at the CERN Large Hadron Collider*", JINST 3 (2008) S08006.
<https://iopscience.iop.org/article/10.1088/1748-0221/3/08/S08006>
- [67] MoEDAL Collaboration, B. Acharya et al., "Search for magnetic monopoles with the MoEDAL prototype trapping detector in 8 TeV proton-proton collisions at the LHC," JHEP 08 (2016) 067.
<https://link.springer.com/article/10.1007%2FJHEP08%282016%29067>
- [68] J. L. Feng, "*FASER and the Search for Light and Weakly Interacting Particles*", Astrophys.Space Sci.Proc. 56 (2019).
<http://inspirehep.net/record/1767324/>
- [69] ALICE Collaboration, F. Noferini, "*ALICE results from Run-1 and Run-2 and perspectives for Run-3 and Run-4*", J. Phys.: Conf. Ser. 1014 012010, 2018.
<https://iopscience.iop.org/article/10.1088/1742-6596/1014/1/012010>
- [70] D. Nouais et al., "*The ALICE Silicon Drift Detector system*", Nuclear Instruments and Methods in Physics Research A 501 (2003) 119–125.
<https://www.sciencedirect.com/science/article/pii/S016890020202020X>
- [71] G. Contin, "*The Silicon Strip Detector (SSD) for the ALICE experiment at LHC: construction, characterization and charged particles multiplicity studies*", Università Degli Studi Di Trieste, 2008.
<http://www.infn.it/thesis/PDF/getfile.php?filename=3305-Contin-dottorato.pdf>
- [72] ALICE Collaboration, "*Technical Design Report of the Time Projection Chamber*", CERN-OPEN-2000-183, CERN-LHCC-2000-001, January, 2000.
<https://cds.cern.ch/record/451098/files/open-2000-183.pdf>
- [73] F. Sauli, "*Principle of Operation of Multiwire Proportional Chamber*", CERN 77-09, 3 May 1977.
<http://cdsweb.cern.ch/record/117989/files/CERN-77-09.pdf>
- [74] ALICE Collaboration, "*Technical Design Report of the Transition Radiation Detector*", ALICE-TDR-9, CERN-LHCC-2001-021, LYCEN-2001-97, October, 2001.
<https://cds.cern.ch/record/519145/files/cer-2275567.pdf>
- [75] ALICE Collaboration, "*Addendum to the Technical Design Report of the Time of Flight System (TOF)*", CERN-LHCC-2002-016, April, 2002.
- [76] ALICE Collaboration, "*Technical Design Report of the Photon Spectrometer (PHOS)*", CERN-LHCC-99-04, March, 1999.
<https://cds.cern.ch/record/381432/files/cer-0307033.pdf>
- [77] ALICE Collaboration, "*Electromagnetic Calorimeter Technical Design Report*", CERN-LHCC-2008-014, CERN-ALICE-TDR-014, September, 2008.
<https://cds.cern.ch/record/1121574/files/ALICE-TDR-014.pdf>

- [78] ALICE Collaboration, "ALICE DCal: An Addendum to the EMCal Technical Design Report Di-Jet and Hadron-Jet Correlation Measurements in ALICE", CERN-LHCC-2010-011, ALICE-TDR-14-add-1, June, 2010.
<http://cds.cern.ch/record/1272952/files/>
- [79] ALICE Collaboration, "Technical Design Report of the High Momentum Particle Identification Detector", CERN-LHCC-98-19, August, 1998.
- [80] T. Ekelof, et al., "The Čerenkov Ring-Imaging Detector: Recent Progress and Future Development", Physica Scripta. Vol. 23,718-726, 1981.
<https://iopscience.iop.org/article/10.1088/0031-8949/23/4B/023>
- [81] ALICE Collaboration, "Technical Design Report on Forward Detectors: FMD, T0 and V0", CERN-LHCC-2004-025, September, 2004.
<http://cds.cern.ch/record/781854/files/>
- [82] ALICE Collaboration, "ALICE Photon Multiplicity Detector (PMD): Technical Design Report", CERN-LHCC-99-032 ; CERN-OPEN-2000-184 ; ALICE-TDR-6, September, 1999.
<http://cds.cern.ch/record/451099/files/>
- [83] ALICE Collaboration, "Addendum to the Technical Design Report of the Photon Multiplicity Detector (PMD)", CERN-LHCC-2003-038, September, 2003.
<http://cds.cern.ch/record/642177/files/>
- [84] ALICE Collaboration, "Addendum to the Technical Design Report of the Dimuon Forward Spectrometer", ALICE-TDR-5-add-1, CERN-LHCC-2000-046, December, 2000.
<http://alice-collaboration.web.cern.ch/sites/alice-collaboration.web.cern.ch/files/documents/TechnicalDesignReport/muon-tdr2.pdf>
- [85] J.-C. Cabanillas-Noris, M. I. Martinez, and I. L. Monzon, "ALICE Diffractive Detector Control System for RUN-II in the ALICE Experiment", J. Phys. Conf. Ser. 761 no. 1, (2016) 012025.
<https://iopscience.iop.org/article/10.1088/1742-6596/761/1/012025>
- [86] J.-P. Revol, E. Calvo Villar, and C. Mayer, "General Characteristics of the AD Detector", Alice public note pub-3033, April, 2016.
- [87] ALICE Collaboration, "Technical Design Report of the Zero Degree Calorimeter (ZDC)", CERN-LHCC-99-05, March, 1999.
<http://cds.cern.ch/record/381433/files/>
- [88] ACORDE Collaboration, A. Fernández et al., "ACORDE a Cosmic Ray Detector for ALICE", Nucl. Instrum. Meth. A572 (2007) 102–103.
<https://www.sciencedirect.com/science/article/pii/S016890020602016X>
- [89] Z. W. Lin and C. M. Ko, "Partonic effects on the elliptic flow at relativistic heavy ion collisions", Phys. Rev. C 65, 034904, 2002.
<https://journals.aps.org/prc/abstract/10.1103/PhysRevC.65.034904>
- [90] Z. W. Lin, C. M. Ko and S. Pal, "Partonic Effects on Pion Interferometry at the Relativistic Heavy-Ion Collider", Phys. Rev. Lett. 89, 152301, 2002.
<https://journals.aps.org/prl/abstract/10.1103/PhysRevLett.89.152301>

- [91] Z. W. Lin and C. M. Ko, "Kaon interferometry at RHIC from the AMPT model", J. Phys. G 30, S263, 2004.
<https://iopscience.iop.org/article/10.1088/0954-3899/30/1/031/meta>
- [92] B. A. Li and C. M. Ko, "Formation of superdense hadronic matter in high energy heavy-ion collisions", Phys. Rev. C 52, 2037, 1995.
<https://journals.aps.org/prc/abstract/10.1103/PhysRevC.52.2037>
- [93] B. A. Li, A. T. Sustich, B. Zhang and C. M. Ko, "Studies Of Superdense Hadronic Matter In A Relativistic Transport Model", Int. J. Mod. Phys. E 10, 267, 2001.
<https://www.worldscientific.com/doi/abs/10.1142/S0218301301000575>
- [94] ALICE Collaboration, B. B. Abelev et al., "Performance of the ALICE Experiment at the CERN LHC", Int. J. Mod. Phys. A29 (2014) 1430044.
<https://arxiv.org/abs/1402.4476>
- [95] R. Frühwirth, "Application of Kalman filtering to track and vertex fitting", Nucl. Instrum. Meth. A262 (1987) 444–450.
<https://www.sciencedirect.com/science/article/pii/S0168900287908874>
- [96] ATLAS Collaboration, J. Jia, "Measurement of elliptic and higher order flow from ATLAS experiment at the LHC", J. Phys. G38 (2011) 124012. <https://arxiv.org/abs/1107.1468>
- [97] K. C. Zapp, "JEWEL 2.0.0 - Directions for Use", Eur.Phys.J. C74, 2762, arXiv:1311.0048, hep-ph, 2014.
<https://arxiv.org/abs/1311.0048>
- [98] G. Bíró et al, "HIJING++, a Heavy Ion Jet INteraction Generator for the High-luminosity Era of the LHC and Beyond", arXiv:1811.02131, physics.comp-ph, 2018.
<https://arxiv.org/abs/1811.02131>
- [99] T. Renk, "YaJEM - a Monte Carlo code for in-medium shower evolution", arXiv:1009.3740, hep-ph, 2010.
<https://arxiv.org/abs/1009.3740>

A Approximation of Medium Formation Timescale Compared to Nuclear Radius

The calculation is done using natural units ($\hbar = c = k$) and the following unit conversion can be used: $1 \text{ eV} = 11600 \text{ K} = 5.07 \cdot 10^6 \text{ m}^{-1} = 1.52 \cdot 10^{15} \text{ s}^{-1}$. Starting from uncertainty principle, we can estimate the formation time of jets and medium since the collisions occurred;

$$\begin{aligned} \Delta p \Delta x = \Delta E \Delta t &\geq \frac{1}{2} \\ t_{jet, QGP} \approx \Delta t &\approx \frac{1}{2E}. \end{aligned} \quad (\text{A.1})$$

The QGP medium's temperature is about 0.47 GeV in ALICE so the formation time of medium t_{QGP} is around 1.064 GeV^{-1} . For the highest $p_T = 25 \text{ GeV}$ in this thesis, $t_{jet} = 0.02 \text{ GeV}^{-1}$. Therefore jets were created before medium. The jets have time interval to escape from nuclear radius before the medium creation. For highest p_T ,

$$t_{escape} = t_{QGP} - t_{jet} \approx 1.044 \text{ GeV}^{-1} = 0.206 \text{ fm}. \quad (\text{A.2})$$

But the nuclear radius is given by equation A.3;

$$R \approx r_o A^{1/3}. \quad (\text{A.3})$$

Only Pb-208 isotope used at LHC so $A = 208$. Taking the value $r_o = 1.2 \text{ fm}$, we have $R \approx 7.12 \text{ fm}$. Since $R > t_{escape}$, even if the jets travel at the speed of light, they are still trapped inside nuclear radius by the time the medium exists, and therefore suffer energy loss. Some jets, however, can escape from nuclear radius if they are formed at peripheral nucleus with distance less than or equal to t_{escape} from the edge of nucleus and travel outward from the center of nucleus.

B Cut-Off Limit of j_T Distributions

It is possible for j_T to be larger than p_{Tt} due to its geometrical property from vector product. For example, in $8 < p_{Tt} < 10$ GeV/c and $0.2 < x_{||} < 0.4$ binning, we take a leading particle with $p_{Tt} = 10$ GeV/c with $x_{||} = 0.2$ because the smallest $x_{||}$ and the largest p_{Tt} will give the largest j_T . Assume the leading particle hit the edge of

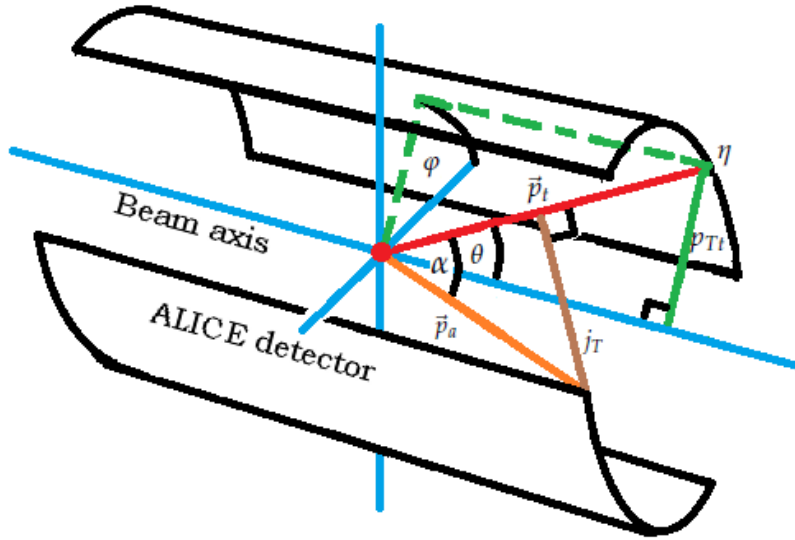


Figure B.1: Illustration of the leading particle (red line) with vector $\vec{p}_t = (p_{Tt}, \eta, \phi)$ and the associated particle (orange line) as they are spotted inside ALICE detector and build-up j_T (brown line).

detector at pseudorapidity $\eta = 0.8$ like in Figure B.1. With relation

$$\theta = 2 \arctan[\exp(-\eta)], \quad (\text{B.1})$$

we can obtain its polar angle $\theta = 0.844$ rad. Since $p_{Tt} = \vec{p}_t \sin(\theta)$, we have \vec{p}_t around 13.74 GeV/c. If the leading particle is paired with an associated particle $\vec{p}_a = 11$ GeV/c, we can find the angle α between two of them from definition of

$$x_{||} = \frac{\vec{p}_t \cdot \vec{p}_a}{|\vec{p}_t|^2} = \frac{|\vec{p}_t| |\vec{p}_a| \cos(\alpha)}{|\vec{p}_t|^2} = \frac{|\vec{p}_a|}{|\vec{p}_t|} \cos(\alpha) \quad (\text{B.2})$$

and get $\alpha = \arccos(x_{||} |\vec{p}_t| / |\vec{p}_a|) = 1.33$ rad. Since

$$j_T = \frac{|\vec{p}_t \times \vec{p}_a|}{|\vec{p}_t|} = \frac{|\vec{p}_t| |\vec{p}_a| \sin(\alpha)}{|\vec{p}_t|} = |\vec{p}_a| \sin(\alpha), \quad (\text{B.3})$$

we can plug α and \vec{p}_a to j_T and get $j_T = 10.67$ GeV/c which is already larger than p_{Tt} . With the same way, we can find the maximum value of j_T analytically by choosing the upper limit for p_a . If we choose maximum $p_a = p_t - 0.01$ GeV/c for the same p_t and $x_{||}$, we will get maximum value of j_T around 13.01 GeV/c.

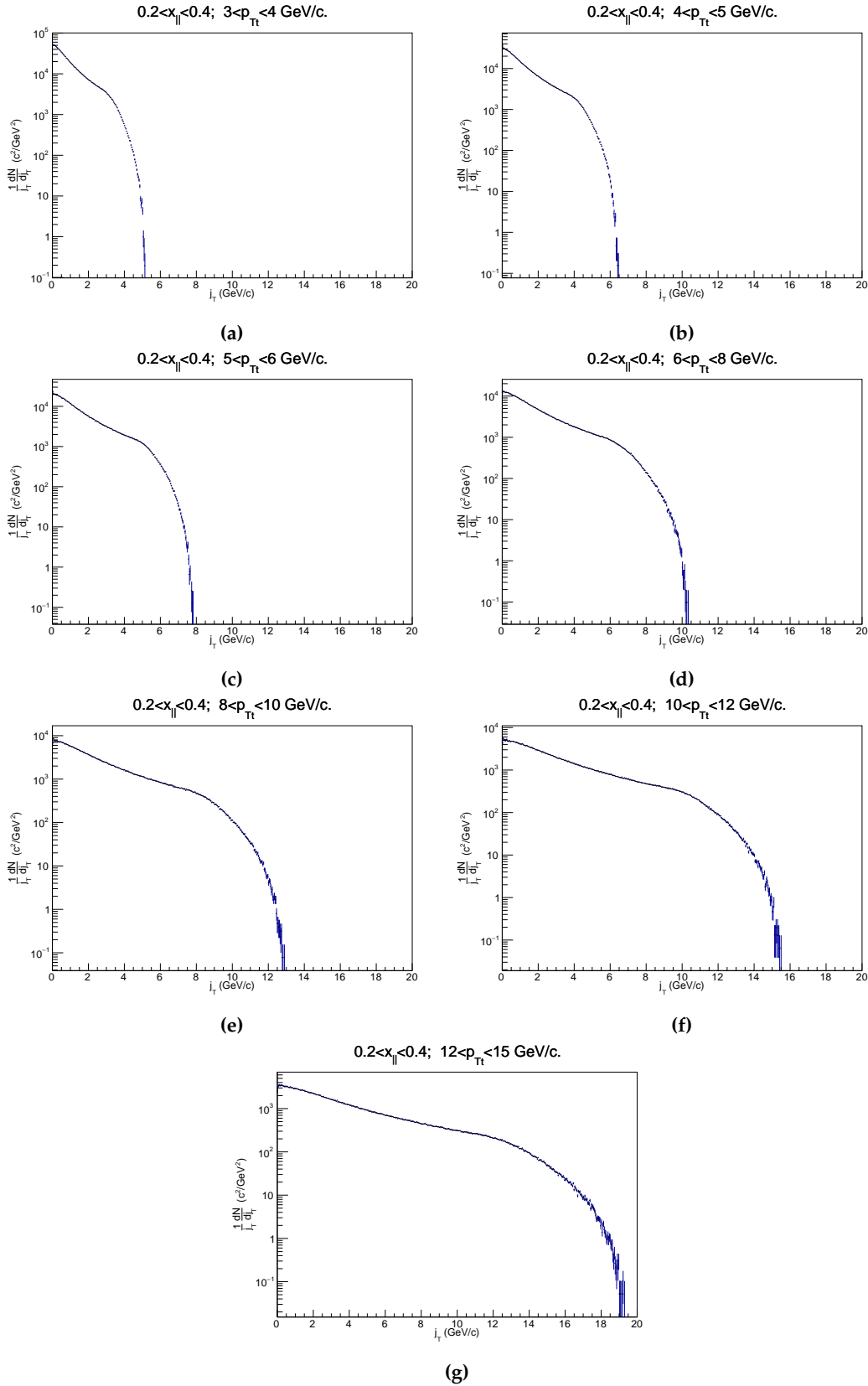
Pairs	$x_{ } \backslash p_{Tt}$	3-4	4-5	5-6	6-8	8-10	10-12	12-15
	10^{10}	$0 < x_{ } < 0.2$	5.26	6.66	7.94	10.58	13.26	15.86
$0.2 < x_{ } < 0.4$		5.14	6.46	7.82	10.34	<u>12.9</u>	15.5	19.3
$0.4 < x_{ } < 0.6$		4.86	5.98	7.18	9.62	11.98	14.38	17.94
$0.6 < x_{ } < 1$		4.14	5.22	6.18	8.42	10.42	12.34	15.46
10^9	$0 < x_{ } < 0.2$	5.06	6.46	7.66	10.06	12.74	15.38	19.3
	$0.2 < x_{ } < 0.4$	4.98	6.06	7.58	9.94	<u>12.34</u>	15.14	18.74
	$0.4 < x_{ } < 0.6$	4.62	5.74	6.98	9.34	11.98	14.06	16.78
	$0.6 < x_{ } < 1$	4.06	4.86	5.86	7.5	9.54	15.66	19.46
10^8	$0 < x_{ } < 0.2$	5.18	6.54	7.9	10.42	12.94	15.86	19.86
	$0.2 < x_{ } < 0.4$	5.1	6.34	7.62	10.18	<u>12.9</u>	15.22	19.18
	$0.4 < x_{ } < 0.6$	4.7	5.86	6.98	9.42	11.58	14.54	17.7
	$0.6 < x_{ } < 1$	4.02	5.06	6.1	8.18	10.18	12.26	14.94

Table B.1: Maximum possible values of j_T from MC toy model.

As comparison to analytical calculation, we can simulate millions of particles pairs with Monte Carlo (MC) method to find out the cut-off limit of j_T in certain p_{Tt} and $x_{||}$ binning. In this toy model, we use vector components $\vec{p} = (p_T, \eta, \varphi)$ to construct particles' momentum. Then p_T, η , and φ for each particle are varied using uniform distribution. Value of p_{Tt} is varied within the given p_{Tt} binning. Pseudorapidity η is randomized from -0.8 to 0.8, and φ vary from zero to 2π . For p_a variation, maximum value $p_t - 0.01$ GeV/c and lower limit 0.1 GeV/c is chosen. From these variables variations, 10^{10} pairs are generated to construct j_T distribution. Variation of one million and ten millions pairs are also explored with this simulation. The number of bins in each histogram is set to 500. The same binning categories $x_{||}$ and p_{Tt} are used in this simulation.

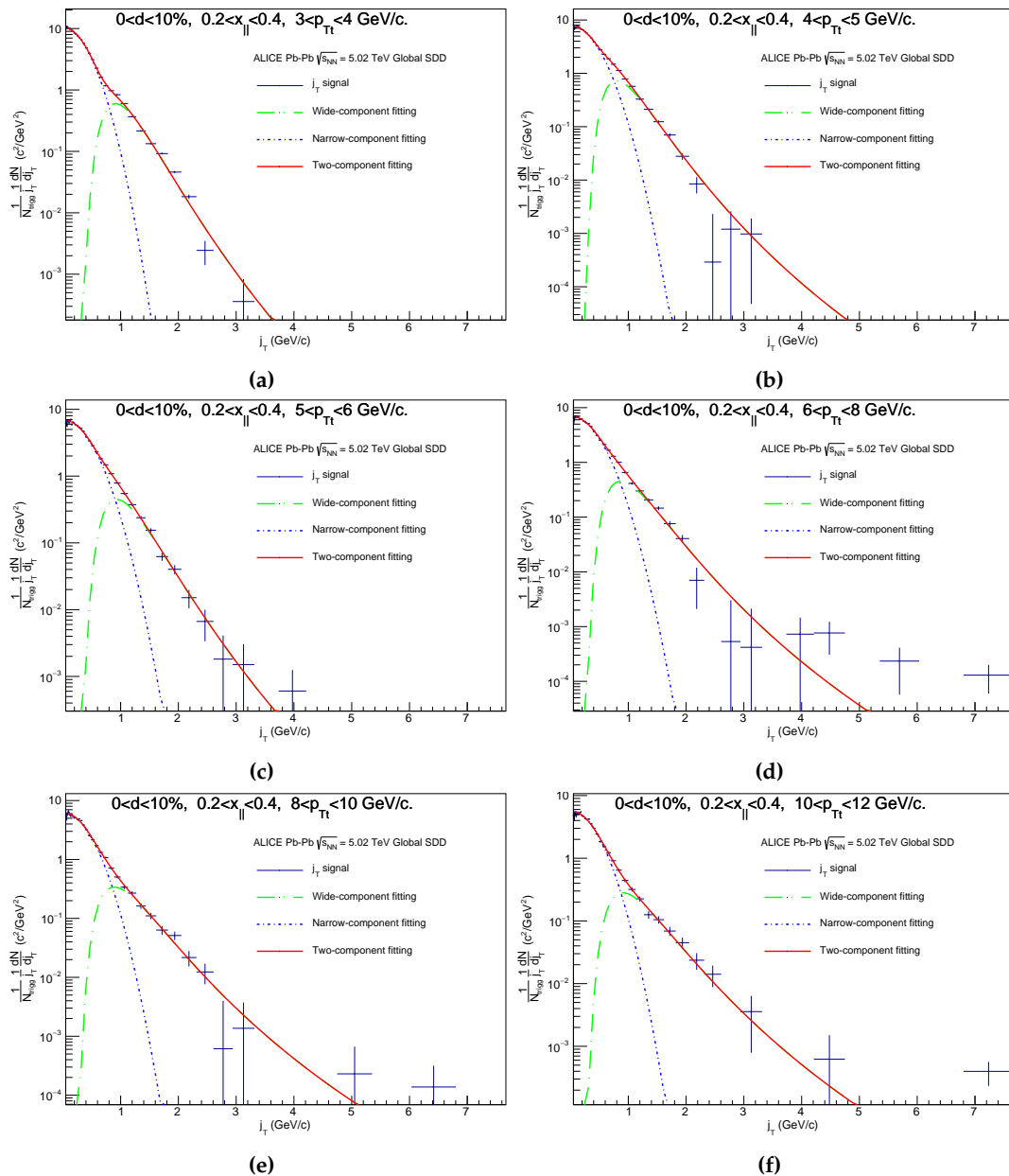
The examples of results are shown in Figure B.2. In this figure, it is clear that there is certain limit to j_T with respect to p_{Tt} . The j_T limits from all $x_{||}$ and p_{Tt} categories are taken from the last non-zero bin center in each histogram and listed in Table B.1. This limit grows as p_{Tt} binning grows and shrinks as $x_{||}$ grows. The results for $15 < p_{Tt} < 18$ and $18 < p_{Tt} < 25$ GeV/c binning are not included since the maximum j_T is already over 20 GeV/c there and thus out of the scope from histogram range.

We can compare the previous analytic result for $p_{Tt} = 10$ GeV/c and $x_{||} = 0.2$ with the underlined numbers in the table. Two out of three number-of-pairs variation shows a very close result to 13 GeV/c. The difference between them may be developed as MC method rely on randomness and there is no associated particle with maximum allowed momentum that fill the distribution. Since the results from simulation are lower than the analytical calculation, they provide stricter limit for j_T . These limits are then applied to signal extraction. Any entries above these limits are discarded since they are not physically possible within the given p_{Tt} and $x_{||}$ binning.

Figure B.2: Toy model for j_T distribution generated by 10^{10} pairs.

C Pb-Pb j_T signal distributions

Figures C.1, C.2, C.3, C.4, C.5, and C.6 are the results of fitting narrow, wide, and two-component to j_T signals in Pb-Pb systems. Discarding entries less than 10 from j_T distributions is applied except for $0.6 < x_{||} < 1$ bin. This is because the j_T distributions in high p_T at $0.6 < x_{||} < 1$ bin is of order of tens. Thus it will be comparable to the size of data and gives significant statistical loss.



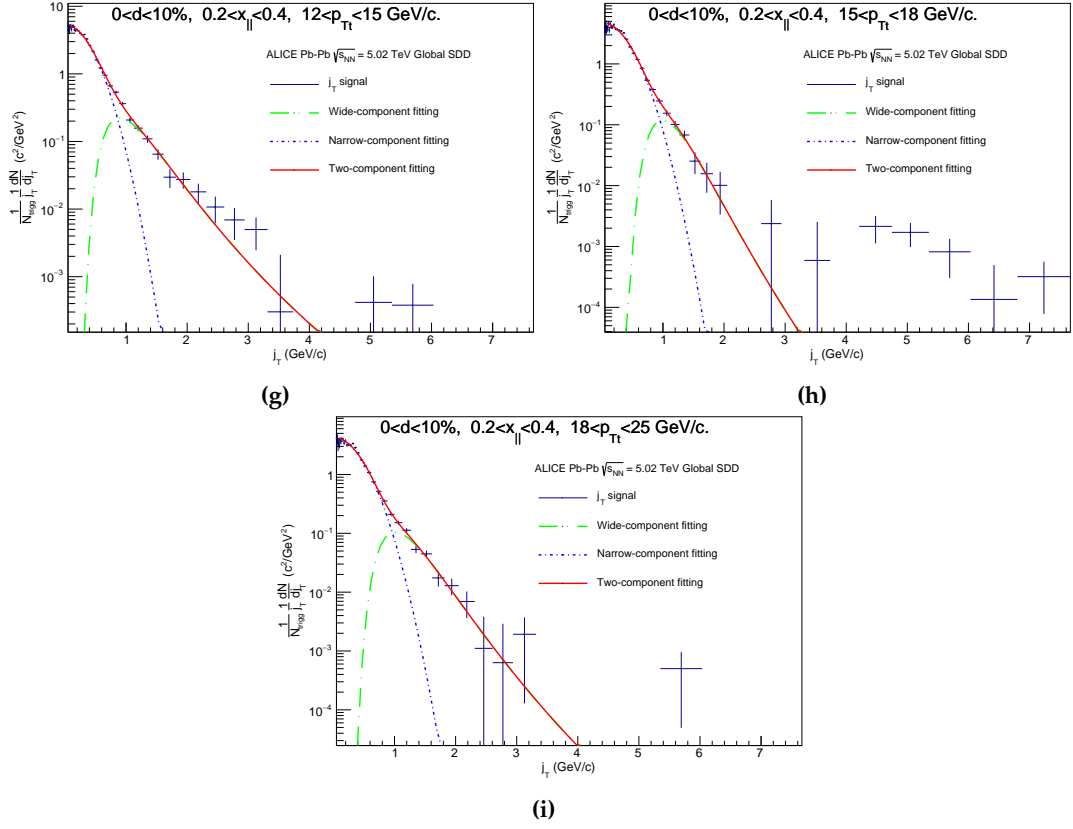
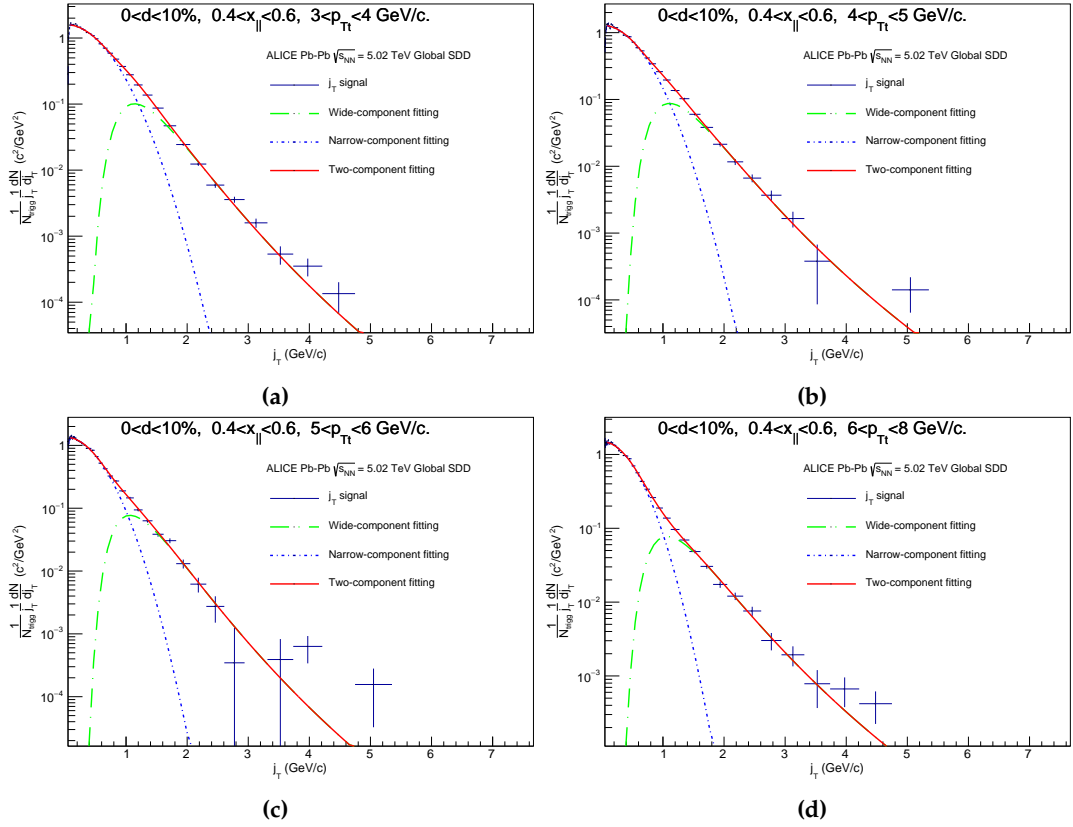
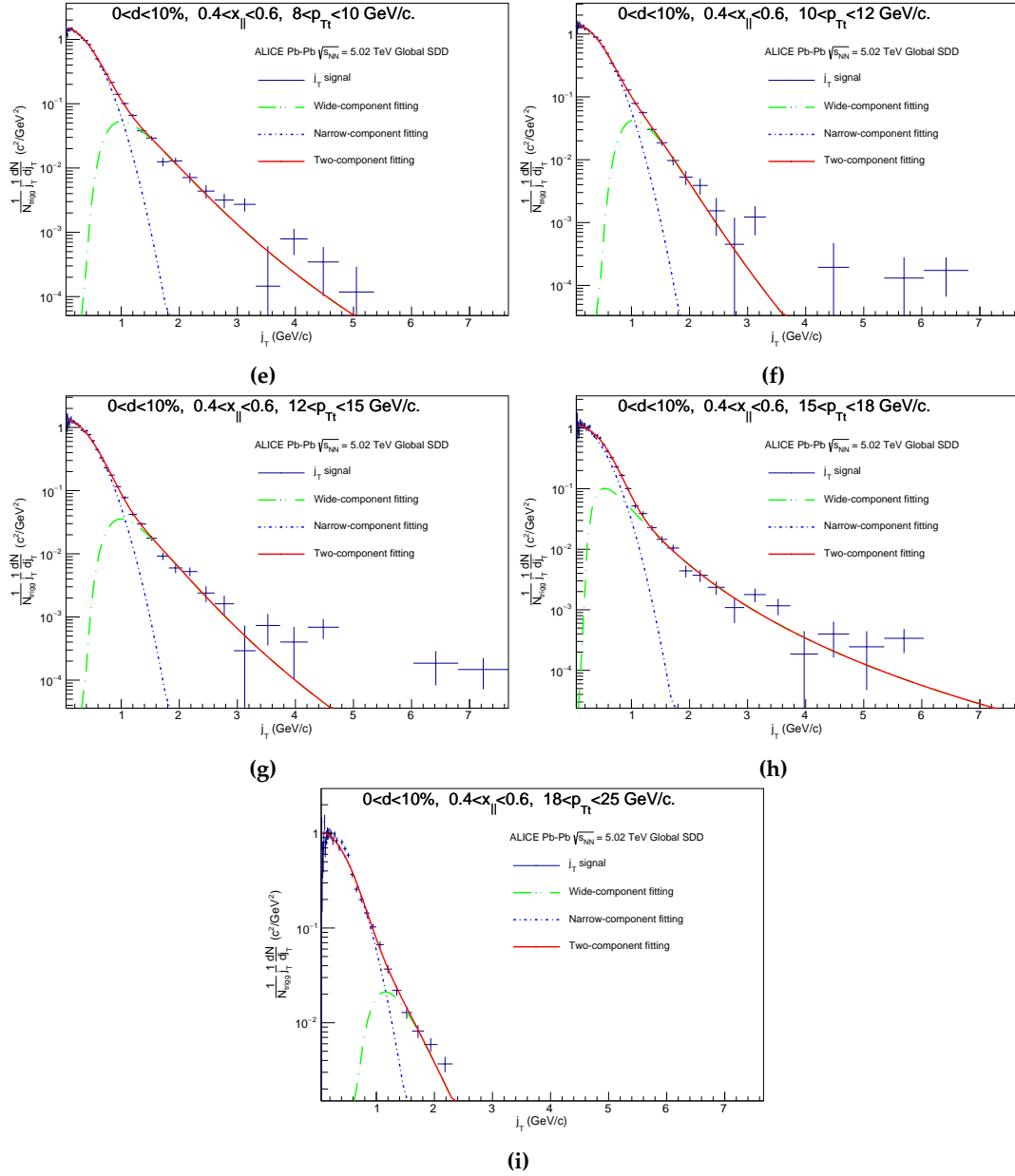
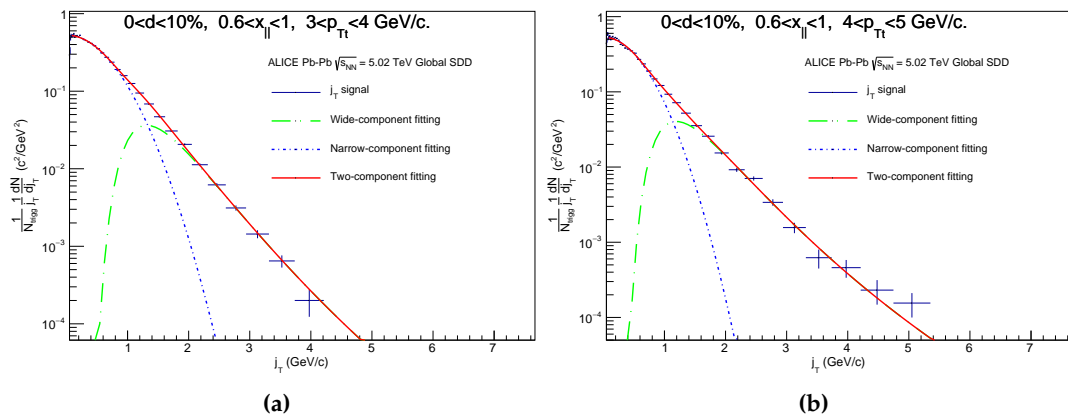


Figure C.1: j_T signals for $0 < d < 10\%$ and $0.2 < x_{||} < 0.4$.



Figure C.2: j_T signals for $0 < d < 10\%$ and $0.4 < x_{||} < 0.6$.

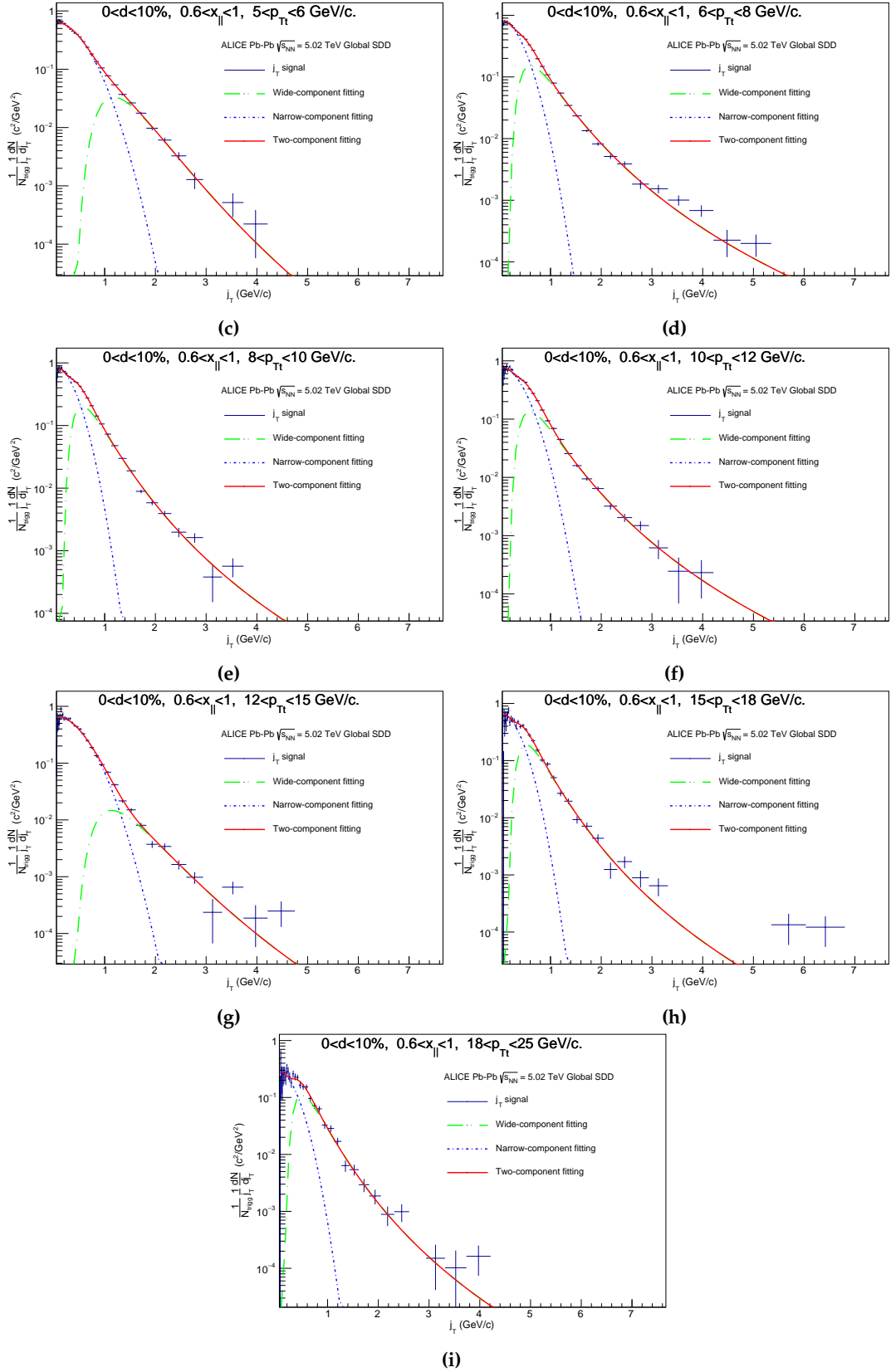
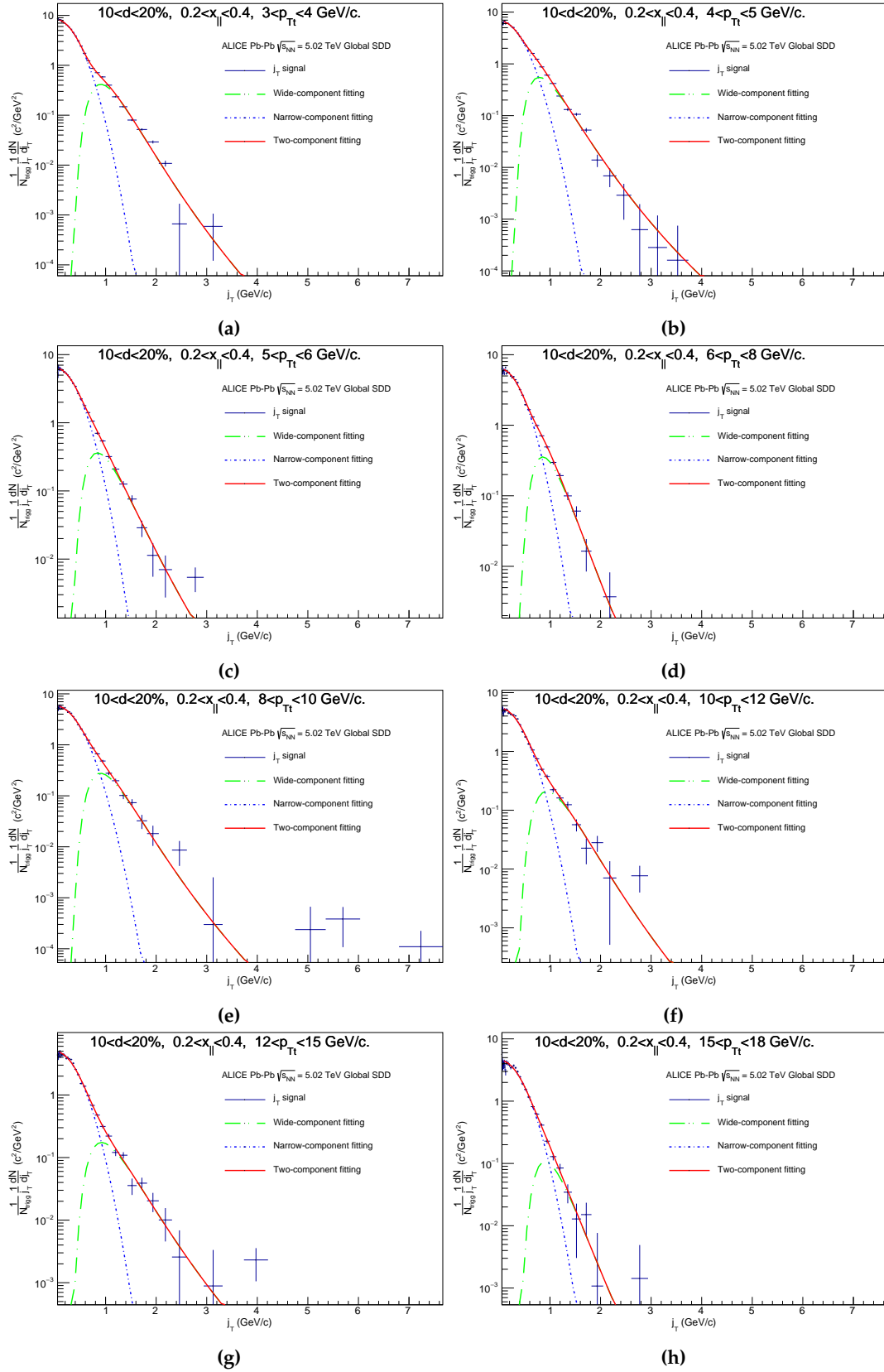
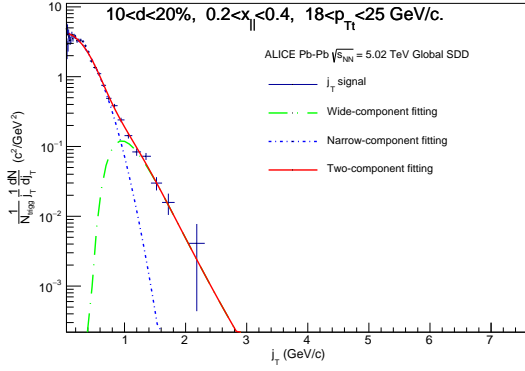
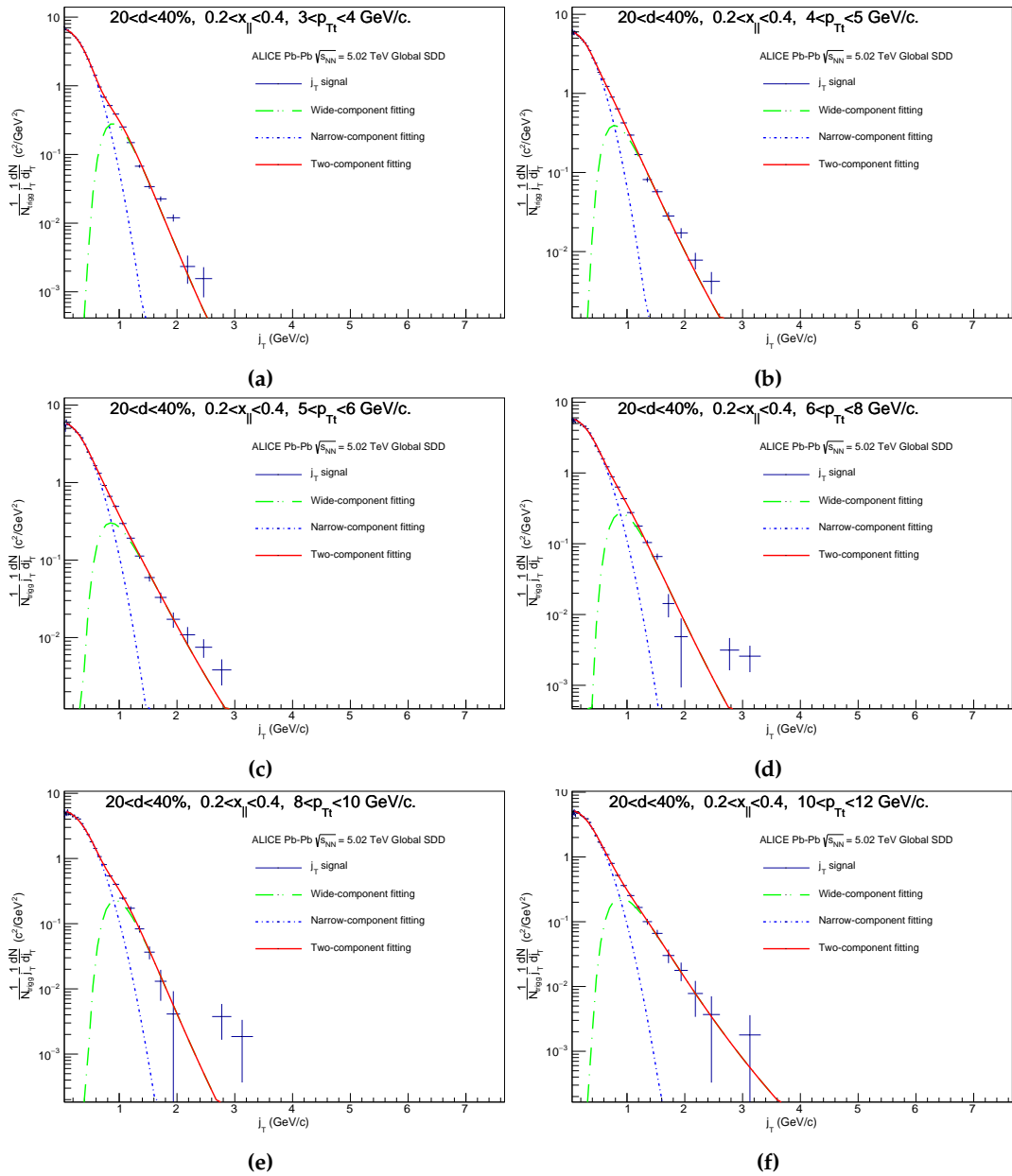


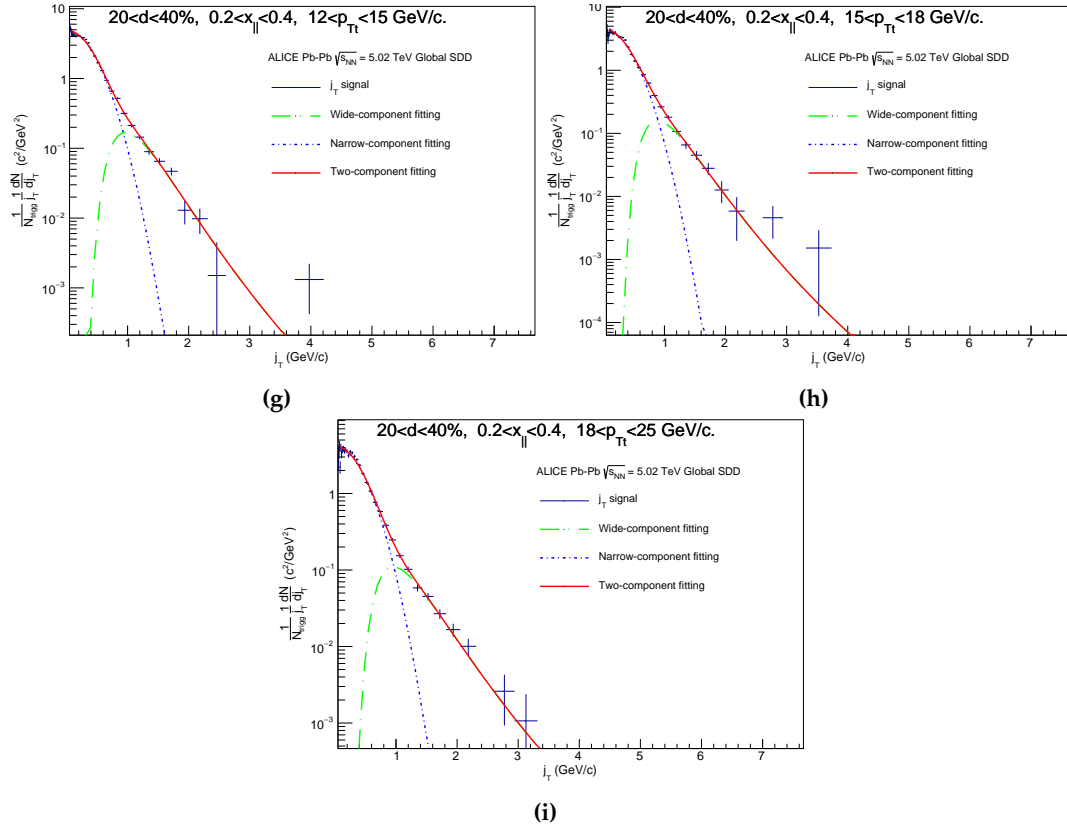
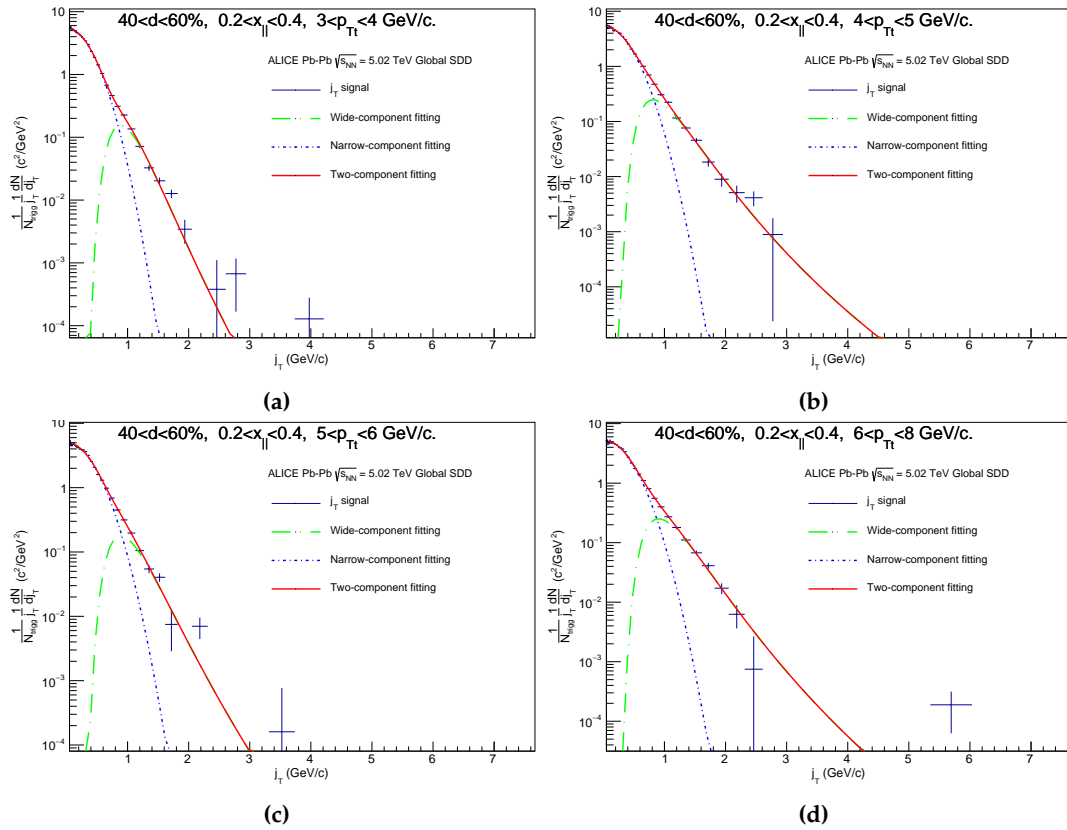
Figure C.3: j_T signals for $0 < d < 10\%$ and $0.6 < x_{||} < 1$.





(i)

Figure C.4: j_T signals for $10 < d < 20\%$ and $0.2 < x_{||} < 0.4$.

Figure C.5: j_T signals for $20 < d < 40\%$ and $0.2 < x_{||} < 0.4$.

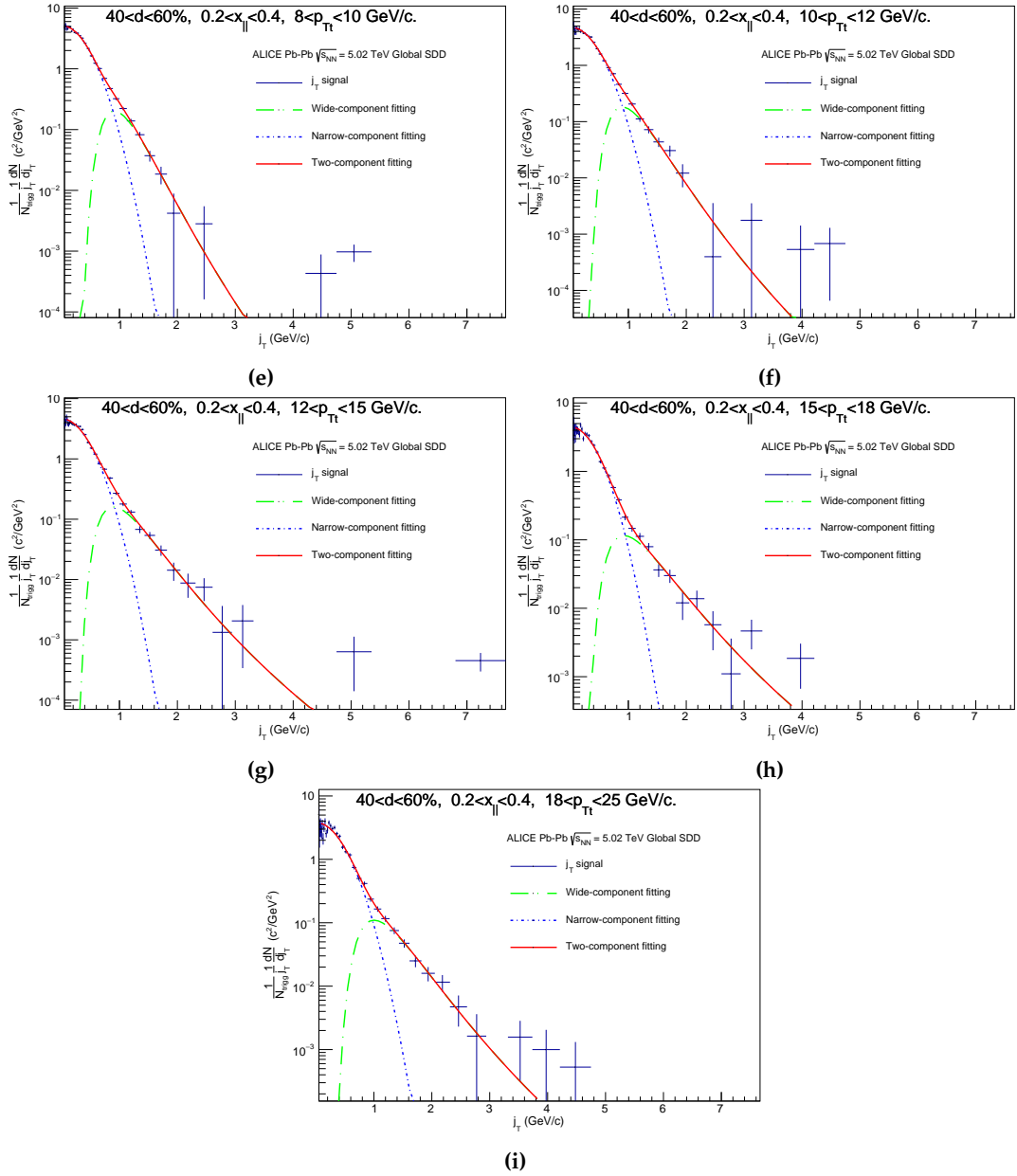


Figure C.6: j_T signals for $40 < d < 60\%$ and $0.2 < x_{||} < 0.4$.